# Data-aided Underwater Acoustic Ray Propagation Modeling

Li Kexin, Mandar Chitre

*Abstract*—**Acoustic propagation models are widely used in numerous oceanic and other underwater applications. Most conventional models are approximate solutions of the acoustic wave equation, and require accurate environmental knowledge to be available beforehand. Environmental parameters may not always be easily or accurately measurable. While data-driven techniques might allow us to model acoustic propagation without the need for extensive prior environmental knowledge, such techniques tend to be data-hungry and often infeasible in oceanic applications where data collection is difficult and expensive. We propose a data-aided ray physics based high frequency acoustic propagation modeling approach that enables us to train models with only a small amount of data. The proposed framework is not only data-efficient, but also offers flexibility to incorporate varying degrees of environmental knowledge, and generalizes well to permit extrapolation beyond the area where data was collected. We demonstrate the feasibility and applicability of our method through four numerical case studies, and one controlled experiment. We also benchmark our method's performance against classical data-driven techniques.**

*Index Terms*—**Acoustic propagation modeling, scientific machine learning, data-efficient acoustic modeling, ocean acoustics, physics-informed machine learning.**

## I. INTRODUCTION

The acoustic propagation in a typical ocean environment exhibits strong spatial and temporal variability. The ability to effectively model ocean acoustic propagation is vital in many oceanic applications, and therefore necessary although often challenging. The multipath structure of an ocean environment leads to complicated constructive and destructive interference patterns, with details that are strongly dependent on the environmental parameters. Given detailed knowledge of the acoustic source and the ocean environment, many popular acoustic propagation models are able to predict spatial variability of the acoustic field in the ocean [1].

Applications related to the acoustic propagation modeling in oceans can be broadly categorized into two main classes: *forward* problems and *inverse* problems. The forward problems seek to estimate the acoustic field at various receiver locations assuming all required environmental parameters are known [2]–[4]. On the other hand, inferring unknown environmental parameters from acoustic measurements is of interest to the inverse problems [5]–[8]. Common inverse problems mainly focus on localization and remote sensing of the ocean environments [9]. As an example, matched field processing (MFP) is a generalized beamforming method which are widely used in the inversion problems. Conventional MFP employs numerical acoustic propagation models to generate field replicas that match to acoustic measurements [10]–[12].

Well-developed numerical propagation models translate our physical understanding of acoustic propagation into mathemat-

ics. Most numerical models are derived from the acoustic wave equation [13]. Closed-form solution to the wave equation are typically analytically intractable in ocean environments, and so the common strategy used by conventional models is to find approximate solutions that work well in many practical applications [14]. There are various widely used approximate solutions to the wave equation, most of which can be seen as variants of the following four groups: ray methods [15], normal modes [16], parabolic equations [17], and wavenumber integration [18].

Variants of the ray method and the method of normal modes are very widely used in most practical ocean acoustic modeling applications. Ray methods solve the wave equation by applying a high-frequency approximation. They track the trajectories of a set of rays originating from the source as they propagate in the ocean. They can be seen as an intuitive way to interpret the solution to the wave equation at high frequencies, where diffraction effects can be neglected. Ray models are computationally efficient and generally suitable for high-frequency applications. An alternative decomposition of the solution to the wave equation leads to the concept of modes. Normal mode methods compute all contributing modes and sum up the collection of modes to estimate the acoustic field at a point. Because the number of modes required for a good approximation grows rapidly with frequency, normal mode models are best suited for lower-frequency applications.

There are two main limitations of the conventional models – computational complexity, and the need for accurate environmental knowledge. While these models are commonly applied in two-dimensional (2D) environments, full three-dimensional (3D) modeling of large-scale environments is often computationally infeasible. Computational capacity has advanced over the years, and there have been advances to solve 3D problems [19]–[22]. Yet, a common approach today is to approximate 3D propagation effects by applying 2D models to $N$ azimuths. This idea is often referred as 2.5D models or $N \times 2$D models in literature [23], [24]. While computationally efficient, 2.5D models can only be applied in environments where the out-of-plane arrival energy is insignificant. Conventional models require accurate environmental knowledge to make good predictions of the acoustic field. Accurate measurement of environmental parameters such as sediment properties, bathymetry, internal waves, suspended bubbles, etc may be difficult or expensive in practice. Even in cases where such information is available, it may not always be straightforward to incorporate the knowledge in the models.

The emergence of data-driven machine learning (ML) algorithms has had a profound impact on many fields [25]. ML algorithms allow computers to automatically learn from

data and perform certain tasks that were previously considered difficult [26]. Many underwater applications may also benefit from the use of ML [27]. For example, ocean acoustic fields may be modeled using classical data-driven ML techniques such as Gaussian process regression (GPR) or neural networks (NN), provided sufficient acoustic field measurements are available as training data for the models. The Gaussian process model is a probabilistic model widely used for regression and classification problems. GPR is capable of capturing relations between inputs and outputs through non-parametric Bayesian inference [28]. Given a set of acoustic measurements and the corresponding measurement locations, GPR can interpolate and extrapolate acoustic predictions with uncertainty distributions at unvisited locations. The computational cost of the traditional GPR scales poorly with the training data size, but sparse GPR models have been proposed to counter such a limitation [29]. The availability of a large amount of accessible datasets has driven the rapid growth in the development of NN learning algorithms over the past years. The universal function approximation theorem establishes that multilayer feed-forward networks have the capability to approximate any continuous function given a sufficient number of hidden units [30]. This suggests that a NNs should be able to approximate the solution to the wave equation by learning appropriate weights from the training data.

Since data-driven approaches only require acoustic measurements for training, they eliminate the need to have full and accurate prior environmental knowledge. However, the two key problems that limit their use in acoustic propagation modeling are the necessity of a large training dataset, and the inability to extrapolate well [31]. The cost of acoustic data acquisition is inevitably high, as the ocean environment tends to be expensive to operate in. In this paper, we address these two problems by developing hybrid methods that not only learn from data, but also utilize the knowledge of the physics of acoustic propagation, without requiring full environmental knowledge. We leverage the complementary strengths of physics-based propagation modeling and data-driven ML to develop a hybrid approach that is computationally efficient, utilizes available environmental knowledge, requires limited data for training, and extrapolates well.

The need to combine knowledge of physics with data-driven ML is not limited to ocean acoustic modeling, and is in fact the focus of an emerging field called *scientific machine learning* (SciML) [32]. Researchers have explored synergistic ways that use scientific domain knowledge to aid data-driven ML [33]–[38]. Data-driven models are trained to learn from the scientific data while respecting certain constraints imposed by our domain knowledge. A popular SciML strategy, named physics-informed neural networks (PINN), imposes physics constraints in the form of partial differential equations (PDE) to act as a regularizer in the loss function of a NN [39]. Such an augmentation in the loss function helps to alleviate the problems of requiring large amounts of data, and the inability to extrapolate. A typical structure of the PINN models is shown in Fig. 1. In the context of acoustic propagation, NNs can be informed by the wave equation to generate data-efficient solution approximations. Work presented in [40]
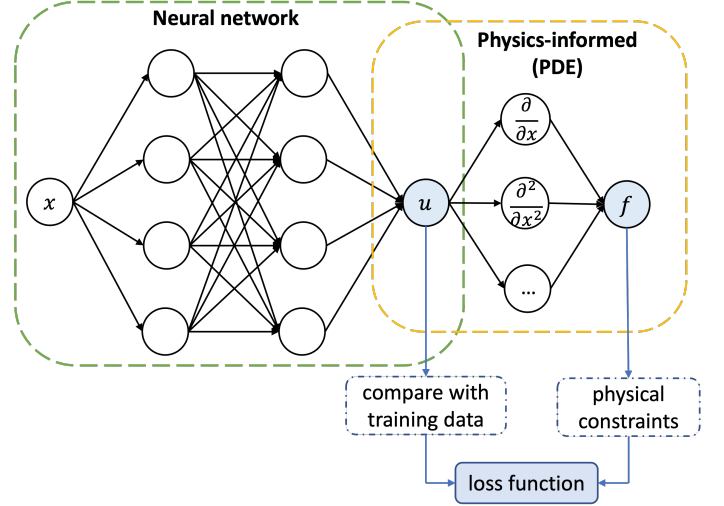


Fig. 1: The typical model structure of PINN.

successfully applies PINN to predict one-dimensional (1D) sound fields with parameterized moving Gaussian sources and impedance boundaries. In the field of medical ultrasound, simulation results in [41] demonstrate that prediction of the 2D acoustic field by the PINN-based methods can be roughly two times faster as compared with the finite difference methods. The authors of [42] adopt PINN to solve the 2D wave equation and propose a curriculum learning based strategy to further improve the convergence rate. In [43], the authors demonstrate that PINN not only can be applied to efficiently solve the forward problems, but may also be helpful in solving inverse problems.

The works reviewed above are not specific to ocean acoustics, and as far as we are aware, there are limited attempts at exploring the use of SciML for ocean modeling. One of the few works that assess the effectiveness of PINN in solving simple ocean-related modeling problems is [44]. Although there are many successful implementations showing that imposing physics knowledge improves model training, the authors of [44] found no significant benefits to the training error by adding the extra physics-informed constraints in the loss function in their simulation studies. They point out that an insufficient amount of training data might be a possible cause. The authors of [45] investigate the benefits of using PINN to solve three ocean modeling related PDEs, including the wave equation. They also study how the weighting of data error and physical constraints in the loss function affect training performance. The authors conclude that the additional physical constraints in the augmented loss function bring more benefits to small datasets.

PINNs encode the physics as part of the loss function, and strike a balance between data-driven and physics-informed through hyper-parameters that control the weights of various terms in the loss function. We take a different approach. We design a class of ML algorithms where the physics is encoded in the structure of the algorithms. The functions these algorithms learn are automatically solutions to the acoustic wave equation. We give up the universal approximation property

of NNs, and instead constrain our algorithms to only learn physically realistic functions. This constraint enables us to learn from very little data, and to extrapolate beyond the region where the data was collected. Our approach is not only data-efficient, but also avoids the need for additional hyper-parameter tuning. Moreover, the algorithm is computationally simple and we are able to fully model 3D acoustic environments easily.

To the best of our knowledge, our previous preliminary work [46] is the first attempt to explore the feasibility of modifying the structures of neurons in a NN in order to incorporate the underlying physics of ocean acoustics propagation. In this follow-up paper, we investigate the idea further and develop a general approach that yields a class of algorithms that are useful for acoustic propagation modeling problems. The main contributions are as follows:

1) We develop a recipe to generate a physics-aided data-driven acoustic propagation model that efficiently solves the acoustic wave equation. The generated model solves the wave equation in a desired number of dimensions (typically 1D, 2D or 3D).
2) The model does not need accurate environmental knowledge, but is able to utilize any available environmental knowledge.
3) The model does not require a large amount of training data, and has the ability to extrapolate beyond the region where data was collected.
4) The recipe supports composition, thus enabling us to combine purely data-driven ML models and physics-aided ML models into a single propagation model. For example, we may use a standard NN to model the reflection coefficient of the seabed, and combine it with a physics-aided model for the overall propagation modeling.
5) Our framework brings interpretability to the trained model parameters, which is particularly useful in inverse problems.
6) We demonstrate our recipe with several numerical experiments, and benchmark it against conventional ML techniques. We also carry out a controlled experiment in a water tank to validate the performance of a generated propagation model.

The rest of the paper is organized as follows. In Section II, we introduce the modeling recipe and illustrate three different formulations arising from the use of the recipe as examples. In Section III, we numerically demonstrate some use-cases of the proposed framework for four common oceanic applications. This is followed by an experimental validation in a water tank environment in Section IV. The field estimation results are benchmarked against a GPR model and a deep neural network (DNN). In Section V, we summarize our findings and discuss potential extensions to the work. Some abbreviations and symbols used throughout the paper are listed in Table I and Table II.

*Notation*: Bold symbols and $[\cdot]$ denote vectors. Symbols in calligraphic font and $(\cdot)$ represent tuples. Sets are written as $\{\cdot\}$. We use the interval notation: $[a, b) = \{x \in \mathbb{R} | a \leqslant x < b\}$. $|c|$ denotes the magnitude of a complex number $c$. For vectors $\boldsymbol{a}$ and $\boldsymbol{b}$, $\boldsymbol{a} \cdot \boldsymbol{b}$ is the dot product. $\|\boldsymbol{a}\|_1$ and $\|\boldsymbol{a}\|_2$ denote $L_1$-norm and $L_2$-norm of vector $\boldsymbol{a}$ respectively. The symbol $\equiv$ denotes equivalence, and the symbol $\nabla^2$ is the Laplace operator.

TABLE I: ABBREVIATIONS USED IN THE PAPER.

| Abbreviation | Description |
|---|---|
| GPR | Gaussian Process Regression |
| ML | Machine Learning |
| NN | Neural Network |
| DNN | Deep Neural Network |
| SciML | Scientific Machine Learning |
| PINN | Physics-Informed Neural Network |
| PDE | Partial Differential Equation |
| AOI | Area Of Interest |
| CW | Continuous Wave |
| RBNN | Ray Basis Neural Network |
| RCNN | Reflection Coefficient Neural Network |
| ISM | Image Source Method |
| RMS | Root Mean Square |
| MATE | Mean Absolute Test Error |

## II. PROBLEM & SOLUTION FORMULATION

### A. Ray-basis Neural Network Framework

We consider an acoustic propagation modeling problem where we have limited environmental knowledge and a small amount of acoustic data collected within area of interest (AOI). We assume an acoustic source is located at position $\boldsymbol{r}_s$ and transmits a continuous wave (CW) signal at frequency $f$ omni-directionally. The signal emitted from the source is scattered by the water surface and other scattering boundaries, as it propagates through the acoustic channel. The received signal $p(\boldsymbol{r})$ at location $\boldsymbol{r}$ is composed of a sum of multipath arrivals, each with its associated intensity and arrival time. The constructive and destructive interference due to the multipath may lead to strong spatial variations in the acoustic field within AOI.

The acoustic wave equation determines the propagation of the acoustic energy from the source, and is expressed as [13]:

$$\frac{\partial^2 p}{\partial t^2} = c^2 \nabla^2 p, \tag{1}$$

where $p$ represents acoustic pressure, $t$ denotes time and $c$ is the sound speed. Assuming a harmonic wave field, a solution to (1) can be written as:

$$p(\boldsymbol{r}, t) = \bar{p}(\boldsymbol{r}) e^{i\omega t}, \tag{2}$$

where $\boldsymbol{r}$ is the spatial coordinate, $\bar{p}(\boldsymbol{r})$ represents complex pressure amplitude, and $\omega = 2\pi f$ denotes angular frequency. Substituting (2) back into (1), and rearranging, we get the Helmholtz equation [13]:

$$k^2 \bar{p}(\boldsymbol{r}) + \nabla^2 \bar{p}(\boldsymbol{r}) = 0 \tag{3}$$

where $k = \frac{\omega}{c}$ is called the wavenumber. Equation (3) can be solved by:

$$\bar{p}(\boldsymbol{r}) = A e^{i\phi} e^{i\boldsymbol{k} \cdot \boldsymbol{r}}, \tag{4}$$

TABLE II: Symbols used in the paper.

| Symbol | Description |
|---|---|
| $\boldsymbol{r}_s$ | Source location |
| $f$ | Frequency |
| $\boldsymbol{r}$ | Spatial coordinate |
| $c$ | Sound speed |
| $\omega$ | Angular velocity |
| $\bar{p}(\boldsymbol{r})$ | Acoustic pressure at location $\boldsymbol{r}$ |
| $k$ | Wavenumber |
| $\boldsymbol{k}$ | Wave propagation vector |
| $A$ | Amplitude of a ray |
| $\phi$ | Phase of a ray |
| $\theta$ | Azimuthal angle |
| $\psi$ | Elevation angle |
| $\bar{d}$ | Propagation distance of a ray |
| $\boldsymbol{r}_o$ | Reference location |
| $\boldsymbol{s}$ | Image source location |
| $d$ | Distance between $\boldsymbol{s}$ and $\boldsymbol{r}_o$ |
| $n_{\text{ray}}$ | Number of arrival rays |
| $n_{\text{ref}}$ | Order of reflection |
| $n_{\text{b}}$ | Number of bottom reflections |
| $n_{\text{s}}$ | Number of surface reflections |
| $e_\theta$ | Error to pre-calculated nominal azimuthal angle $\theta'$ |
| $e_\psi$ | Error to pre-calculated nominal elevation angle $\psi'$ |
| $e_d$ | Error to pre-calculated nominal distance $d'$ |
| $\boldsymbol{r}_{\text{train}}$ | Measurement locations in training dataset |
| $\boldsymbol{y}_{\text{train}}$ | Acoustic measurements in training dataset |
| $\alpha$ | Penalty coefficient of arrival ray amplitude |
| $\zeta$ | Penalty coefficient of angular error |
| $\beta$ | Penalty coefficient of distance error |
| $\eta$ | Penalty coefficient of reflection energy |
| $\mathcal{T}$ | Trainable parameters in RBNN model |
| $\boldsymbol{R}$ | Trainable parameters in RCNN model |
| $\epsilon$ | Reflection coefficient |
| $\kappa$ | Reflection phase shift |
| $\gamma$ | Incident angle of a reflection |
| $\Gamma$ | Complex reflection coefficient |
| $l_{\text{a}}$ | Volume absorption loss term |
| $l_{\text{rc}}$ | Reflection loss term |
| $l_{\text{g}}$ | Geometric spreading loss term |

where $A$ and $\phi$ represent amplitude and phase of a wave, and $\boldsymbol{k}$ is wave propagation vector that satisfies:

$$\|\boldsymbol{k}\|_2 = k. \tag{5}$$

Any function of the form (4) solves the wave equation. Due to linearity of the wave equation, the superposition of $n_{\text{ray}}$ such functions must also be a solution to the wave equation. Thus, the field at a location $\boldsymbol{r}$ can be expressed as the sum of terms given by (4):

$$\bar{p}(\boldsymbol{r}) = \sum_{m=1}^{n_{\text{ray}}} A_m e^{i\phi_m} e^{i\boldsymbol{k}_m \cdot \boldsymbol{r}}, \tag{6}$$

where $A_m$ denotes the amplitude of $m^{\text{th}}$ arrival, $\phi_m$ refers to the corresponding phase term, and $\boldsymbol{k}_m = k\hat{\boldsymbol{k}}_m$ for some unit vector $\hat{\boldsymbol{k}}_m$.
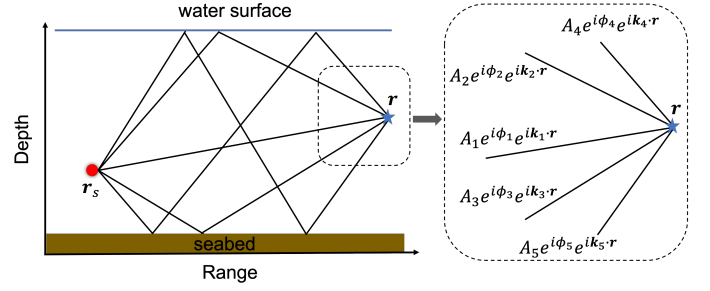


Fig. 2: An example showing the superposition of 5 multipath arrivals at a receiver location in a typical ocean environment.
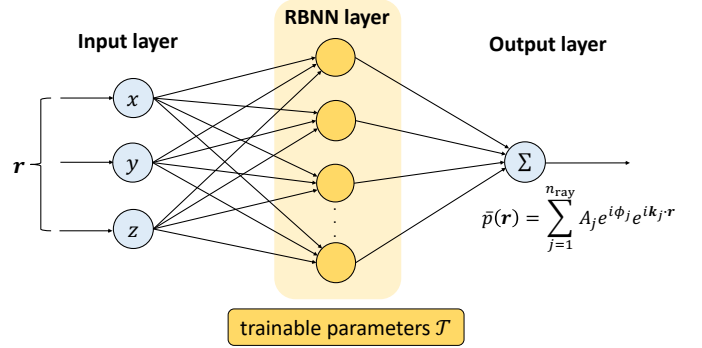


Fig. 3: The computation graph for (6) illustrating the proposed RBNN framework.

This is the well-known ray solution to the acoustic wave equation [15], with $A_m e^{i\phi_m}$ being the complex amplitude of the $m^{\text{th}}$ ray and $\hat{\boldsymbol{k}}_m$ being the direction of travel of that ray. Fig. 2 elaborates the intuition behind (6) from a receiver point of view. The acoustic field at a receiver location $\boldsymbol{r}$ can be visualized as the superposition of $n_{\text{ray}}$ multipath arrivals. Conventional ray models determine $A_m$, $\phi_m$ and $\boldsymbol{k}_m$ for all $m$, given detailed environmental knowledge. It is not generally possible to compute $A_m$, $\phi_m$ and $\boldsymbol{k}_m$ if partial or no environmental knowledge is available. Fortunately, ML provides us the necessary tools to learn the unknown parameters or functions from data. We can think of (6) as a function to be modeled using a specialized NN with each term in the summation playing the role of a neuron (with parameters closely related to $A_m$, $\phi_m$ and $\boldsymbol{k}_m$). The values of the parameters can be learnt from data using a generalized *backpropagation* algorithm [47] with automatic differentiation [48] applied to this NN, such as ADAM [49].

The functions that this NN can learn are guaranteed to solve the wave equation (1) by construction, hence incorporating the acoustic domain knowledge in the structure of the NN. We term this specialized NN as a *ray basis neural network* (RBNN), as the neurons in the network can be interpreted as acoustic rays arriving at a given receiver location as shown in Fig. 3.

It is worth noting that our model structure is determined based on the governing physics and is conceptually different from a conventional PINN. Instead of imposing physical

constraints using the loss function of a standard NN, we embed the constraints in the structure of the NN by making each neuron individually obey the governing physics. We then borrow the training strategies from a standard NN to find the best-fitting values of the unknown parameters of the resulting model by continuously minimizing a loss function that measures the error between the model output and observed data. The dataset used in model training stage is comprised of a set of measurement locations $\boldsymbol{r}_{\text{train}}$ and corresponding acoustic field measurements $\boldsymbol{y}_{\text{train}}$. Furthermore, one can construct more sophisticated NNs with a mix of standard neurons and RBNN-neurons, as we shall show later. Such NNs can be useful in solving problems with partial environmental knowledge.

The formulation presented above forms a basic recipe to model high-frequency acoustic propagation using the SciML methodology. The exact calculations of $A_m$, $\phi_m$ and $\boldsymbol{k}_m$ of each ray are application-dependent, since some of these terms may be calculated based on environmental knowledge, and others determined from parameters learned from data. In Sections II-B and II-C, we apply the recipe to generate models to handle three different application scenarios: plane wave (far-field propagation), spherical wave (near-field propagation) without knowledge of geometry, and spherical wave with knowledge of geometry. In each scenario, the exact details of RBNN-neurons change, but the overall RBNN structure and the training process remains the same.

### B. Plane wave RBNN

In the far-field of a point source, a ray arrival can be well approximated by a planar wavefront. So, if the AOI is sufficiently far from the source, we can use a plane wave formulation for the unknowns in (6). This formulation does not require any prior environmental knowledge, and is particularly helpful to model practical scenarios where the environment is largely unknown. The unknown terms $A_m$ and $\phi_m$ are treated as unknown model parameters to be determined during training. If the sound speed or frequency is unknown, $k$ may also be treated as an unknown parameter. The unit vector $\hat{\boldsymbol{k}}_m$ is parametrized in terms of azimuthal angle $\theta_m$ and elevation angle $\psi_m$:

$$\hat{\boldsymbol{k}}_m = \begin{bmatrix} \cos(\theta_m)\,\sin(\psi_m) \\ \sin(\theta_m)\,\sin(\psi_m) \\ \cos(\psi_m) \end{bmatrix}. \tag{7}$$

The set of trainable RBNN model parameters in the plane wave formulation therefore is:

$$\mathcal{T}_{\text{p}} \equiv \{\boldsymbol{A}, \boldsymbol{\phi}, k, \boldsymbol{\theta}, \boldsymbol{\psi}\}, \tag{8}$$

where $\boldsymbol{A} = [A_1, A_2, \ldots, A_{n_{\text{ray}}}]$, $\boldsymbol{\phi} = [\phi_1, \phi_2, \ldots, \phi_{n_{\text{ray}}}]$, $\boldsymbol{\theta} = [\theta_1, \theta_2, \ldots, \theta_{n_{\text{ray}}}]$ and $\boldsymbol{\psi} = [\psi_1, \psi_2, \ldots, \psi_{n_{\text{ray}}}]$. The pressure amplitude predicted at location $\boldsymbol{r}$ can be expressed as:

$$\bar{p}(\boldsymbol{r}) = \left| \sum_{m=1}^{n_{\text{ray}}} A_m e^{i\phi_m} e^{i\boldsymbol{k}_m \cdot \boldsymbol{r}} \right|. \tag{9}$$

Since we do not assume detailed environmental information, the number of rays $n_{\text{ray}}$ is unknown, but a conservative upper bound can often be estimated. Nevertheless, we find it better

to think of $n_{\text{ray}}$ as a model hyper-parameter to be tuned during training, with the tuning guided by an estimate, if available. Due to the strongly non-linear effect of parameters $\theta_m$ and $\psi_m$, the RNBB may get trapped in local minima or saddle points during training if $n_{\text{ray}}$ is small. A large $n_{\text{ray}}$ and uniformly distributed random initialization of $\boldsymbol{\theta}$ and $\boldsymbol{\psi}$ ensures better convergence, but creates potential for overfitting. A $L_1$-norm regularization on parameters $\boldsymbol{A}$ encourages sparsity, i.e., a trained model with only a small number of rays, and therefore avoids overfitting.

The loss function we minimize during the training is therefore the sum-square difference in predicted and measured pressure amplitudes at given receiver locations, combined with the $L_1$-norm regularization term to encourage sparsity:

$$L_{\text{p}}(\boldsymbol{r}, y; \mathcal{T}_{\text{p}}) = |\bar{p}(\boldsymbol{r}) - y|^2 + \alpha \, \|\boldsymbol{A}\|_1, \tag{10}$$

where $y$ is the observed pressure amplitude at location $\boldsymbol{r}$, and $\alpha$ is a hyper-parameter that controls the regularization. While we write (10) for a single training data point, it is usually summed over a training mini-batch as per the standard practice in ML [50]. During validation and model evaluation, $\alpha$ is set to 0.

### C. Spherical wave RBNN

The acoustic propagation near a point source is best modeled using spherical waves. In a typical ocean environment, there are three key factors that contribute to the overall transmission loss: geometric spreading loss $l_{\text{g}}$, volume absorption loss $l_{\text{a}}$ and reflection loss $l_{\text{rc}}$ (net effect from all reflecting boundaries). In contrast to the plane wave formulation, the amplitude $\bar{A}$ and phase $\bar{\phi}$ of an arrival ray in our spherical wave formulation are functions of both source location $\boldsymbol{r}_{\text{s}}$ and receiver location $\boldsymbol{r}$. Therefore, (6) is re-written as:

$$\bar{p}(\boldsymbol{r}) = \sum_{m=1}^{n_{\text{ray}}} \bar{A}_m(\boldsymbol{r}_{\text{s}}, \boldsymbol{r}) e^{i\bar{\phi}_m(\boldsymbol{r}_{\text{s}}, \boldsymbol{r})}, \tag{11}$$

where

$$\bar{A}_m(\boldsymbol{r}_{\text{s}}, \boldsymbol{r}) = l_{\text{g}}^m(\boldsymbol{r}_{\text{s}}, \boldsymbol{r}) l_{\text{rc}}^m(\boldsymbol{r}_{\text{s}}, \boldsymbol{r}) l_{\text{a}}^m(\boldsymbol{r}_{\text{s}}, \boldsymbol{r}), \tag{12a}$$

$$\bar{\phi}_m(\boldsymbol{r}_{\text{s}}, \boldsymbol{r}) = \phi_{\text{rc}}^m(\boldsymbol{r}_{\text{s}}, \boldsymbol{r}) + k\bar{d}_m(\boldsymbol{r}_{\text{s}}, \boldsymbol{r}). \tag{12b}$$

Here, $\phi_{\text{rc}}^m(\boldsymbol{r}_{\text{s}}, \boldsymbol{r})$ is the overall reflection phase shift along the trajectory of the $m^{\text{th}}$ ray, and $k\bar{d}_m(\boldsymbol{r}_{\text{s}}, \boldsymbol{r})$ corresponds to the phase change for a propagation distance of $\bar{d}_m(\boldsymbol{r}_{\text{s}}, \boldsymbol{r})$. The 3D spherical geometric spreading loss is [51]:

$$l_{\text{g}}^m(\boldsymbol{r}_{\text{s}}, \boldsymbol{r}) = \frac{1}{\bar{d}_m(\boldsymbol{r}_{\text{s}}, \boldsymbol{r})}. \tag{13}$$

The volume absorption loss generally depends on the operating frequency, propagation distance and characteristics of the propagating medium. The widely used simplified expression of the attenuation per unit distance due to volume absorption is given in [52]. The attenuation and phase shift when sound interacts with scattering boundaries (e.g. seabed) can also be calculated if we know the angle of interaction and the properties and structure of the boundary [53].

The spherical wave formulation can incorporate varying degrees of environmental knowledge. The model parameters
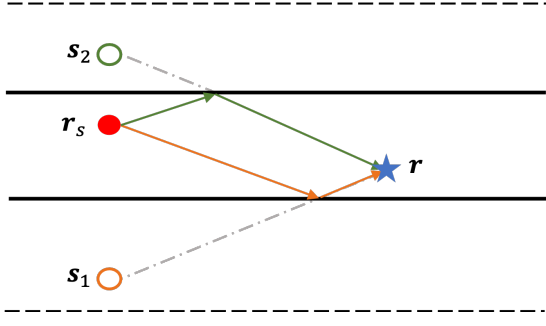
Fig. 4: An illustration showing two image sources corresponding to two reflected ray paths between the source and the receiver.

involved in the field prediction can be found through either data-driven learning strategies or numerical calculations, depends on the environmental knowledge provided. We next illustrate two examples that correspond to the scenarios with and without knowledge of the channel geometry:

*1) Without knowledge of channel geometry:* For the scenarios where the channel geometry is largely unknown, the trajectories of rays from the source to the receiver are unknown. However, applying the image source method (ISM) [54] to the problem, we can replace the unknown source location and channel geometry by a set of unknown image sources as illustrated in Fig. 4. The problem then reduces to finding the parameters of the unknown image sources to match with the training data.

Let $\boldsymbol{r}_o$ be an arbitrary reference position within the AOI. We can parametrize each images source by a pressure amplitude $A_m$, phase $\phi_m$, a direction vector (corresponding to azimuthal angle $\theta_m$ and elevation angle $\psi_m$) and distance $d_m$ from this reference position. In the case of an isovelocity environment, the pressure amplitude at a receiver $\boldsymbol{r}$ is then given by:

$$\bar{p}(\boldsymbol{r}) = \left| \sum_{m=1}^{n_{\text{ray}}} A_m \frac{l_{\text{a}}(\|\boldsymbol{s}_m - \boldsymbol{r}\|_2)}{\|\boldsymbol{s}_m - \boldsymbol{r}\|_2} e^{i(\phi_m + k\|\boldsymbol{s}_m - \boldsymbol{r}\|_2)} \right|, \quad (14)$$

where:

$$\boldsymbol{s}_m = \boldsymbol{r}_o - d_m \begin{bmatrix} \cos(\theta_m)\,\sin(\psi_m) \\ \sin(\theta_m)\,\sin(\psi_m) \\ \cos(\psi_m) \end{bmatrix} \quad (15)$$

and $l_{\text{a}}(\cdot)$ is attenuation due to volume absorption as given in [52]. The complete set of trainable parameters for this model are:

$$\mathcal{T}_{\text{s}} \equiv (k, \boldsymbol{\theta}, \boldsymbol{\psi}, \boldsymbol{d}, \boldsymbol{A}, \boldsymbol{\phi}). \quad (16)$$

and the loss function to be minimized is identical to (10).

*2) With knowledge of channel geometry:* If the channel geometry and associated reflecting boundaries are partially or completely known, we can incorporate available knowledge in our model. To illustrate the idea, let us assume that we know the source location and the channel geometry. We also assume that the sea surface is modeled well as a pressure-release boundary, but that we do not know the reflection coefficient for the seabed.

Given the source location and channel geometry, we can compute the incidence angle $\gamma_m$ for each ray at the seabed.

The reflection coefficient of the seabed is an unknown function of incidence angle, and may be modeled using a simple 1-input 2-output (magnitude and phase) feedforward NN with a single hidden layer. We call this NN as the *reflection coefficient neural network* (RCNN). The same reflection coefficient function applies to all rays incident on the seabed, and hence the RCNN weights are shared across all the rays. The RCNN is implemented as an additional layer in the RBNN framework with shared weights, as illustrated in Fig. 5.

A ray may experience more than one reflections at the seabed. The overall reflection coefficient for $m^{\text{th}}$ arrival ray is:

$$l_{\text{rc}}^m(\boldsymbol{r}) = \prod_{i=1}^{n_{\text{b}}^m} \text{RCNN}_\epsilon(\gamma_i^m(\boldsymbol{r})), \quad (17)$$

where $n_{\text{b}}^m$ is the number of seabed reflections for ray $m$, $\gamma_i^m(\cdot)$ is the incidence angle for reflection $i$, and $\text{RCNN}_\epsilon(\cdot)$ is the predicted reflection coefficient magnitude from the RCNN. The corresponding cumulative phase shift is:

$$\phi_{\text{rc}}^m(\boldsymbol{r}) = n_{\text{s}}^m \pi + \sum_{i=1}^{n_{\text{b}}^m} \text{RCNN}_\kappa(\gamma_i^m(\boldsymbol{r})), \quad (18)$$

where $\text{RCNN}_\kappa(\cdot)$ is the reflection phase shift predicted by the RCNN, and $n_{\text{s}}^m$ is the number of surface reflections for ray $m$. The phase change $n_{\text{s}}^m \pi$ is due to the pressure-release boundary assumption, and can easily be replaced by a more sophisticated surface reflection model, if desired.

As in the previous section, we choose to apply the ISM to replace the source with multiple image sources. This allows us to work with approximate knowledge of channel geometry and learn the exact locations of the image sources from data, as we illustrate later in this section. The resultant pressure amplitude can be expressed as:

$$\bar{p}(\boldsymbol{r}) = \left| \sum_{m=1}^{n_{\text{ray}}} \frac{l_{\text{rc}}^m(\boldsymbol{r}) l_{\text{a}}(\|\boldsymbol{s}_m - \boldsymbol{r}\|_2)}{\|\boldsymbol{s}_m - \boldsymbol{r}\|_2} e^{i(\phi_{\text{rc}}^m(\boldsymbol{r}) + k\|\boldsymbol{s}_m - \boldsymbol{r}\|_2)} \right|, \quad (19)$$

where the ray trajectory necessary for the evaluation of $l_{\text{rc}}^m(\cdot)$ can be computed by geometric ray tracing. Since we are using a ray tracing model, the recipe also works with non-isovelocity sound speed profile by changing the euclidean distances term $\|\boldsymbol{s}_m - \boldsymbol{r}\|_2$ in (19) to actual propagation distances along the curved ray paths.

The overall computation graph for (19) can be viewed as a NN with geometric ray tracer, RCNN layer, and RBNN layer as shown in Fig. 5. The set of trainable RBNN parameters in this model are:

$$\mathcal{T}_{\text{sg}} \equiv (k, \boldsymbol{\theta}, \boldsymbol{\psi}, \boldsymbol{d}, \boldsymbol{R}), \quad (20)$$

where $\boldsymbol{R}$ represents all trainable parameters in the RCNN layer.

The search spaces for $\boldsymbol{\theta}$ and $\boldsymbol{\psi}$ span $[0, 2\pi)$, and for $\boldsymbol{d}$ spans $[0, \infty)$. The knowledge of geometry and the source location allows us to pre-calculate nominal arrival ray directions $\boldsymbol{\theta}'$, $\boldsymbol{\psi}'$ and propagation distances $\boldsymbol{d}'$ prior to the model training stage. The calculated nominal directions and distances may deviate from reality due to limited knowledge or measurement error. We model this with appropriate error terms $\boldsymbol{e}_\theta$, $\boldsymbol{e}_\psi$ and $\boldsymbol{e}_d$:
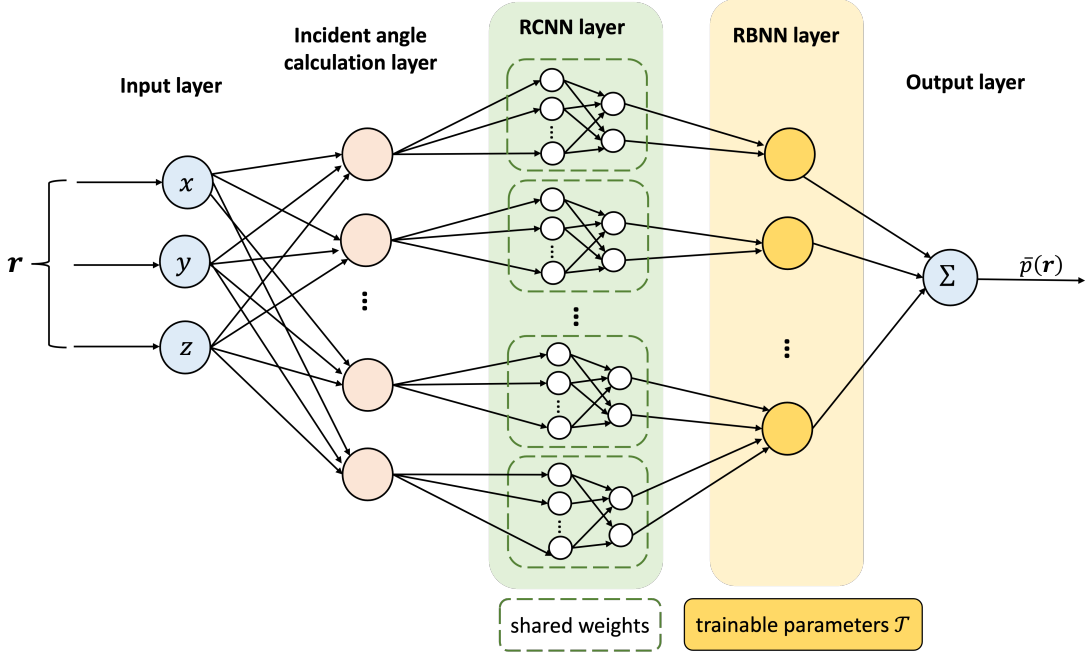
Fig. 5: The computational graph for (19) can be modeled as an additional RCNN layer prior to the RBNN layer.

$$\boldsymbol{\theta} = \boldsymbol{\theta}' + \boldsymbol{e}_\theta, \tag{21a}$$

$$\boldsymbol{\psi} = \boldsymbol{\psi}' + \boldsymbol{e}_\psi, \tag{21b}$$

$$\boldsymbol{d} = \boldsymbol{d}' + \boldsymbol{e}_d. \tag{21c}$$

We then replace the trainable parameters $\boldsymbol{\theta}$, $\boldsymbol{\psi}$, and $\boldsymbol{d}$ with the corresponding error terms, thus replacing (20) with:

$$\mathcal{T}_{\text{sg}} \equiv (k, \boldsymbol{e}_\theta, \boldsymbol{e}_\psi, \boldsymbol{e}_d, \boldsymbol{R}). \tag{22}$$

The amount of error allowed in $\boldsymbol{e}_\theta$, $\boldsymbol{e}_\psi$ and $\boldsymbol{e}_d$ reflect how confident we are about our knowledge of the channel geometry and source location. We impose $L_2$-norm penalty terms in the loss function to constrain values of $\boldsymbol{e}_\theta$, $\boldsymbol{e}_\psi$ and $\boldsymbol{e}_d$ learnt during the training process. We also add a harsh penalty term to ensure that reflection model learnt by the RCNN obeys energy conservation. The resulting loss function is:

$$L_{\text{sg}}(\boldsymbol{r}, y; \mathcal{T}_{\text{sg}}) = |\bar{p}(\boldsymbol{r}) - y|^2 + \left\| \boldsymbol{\zeta}(\boldsymbol{e}_\theta{}^2 + \boldsymbol{e}_\psi{}^2) \right\|_2$$
$$+ \beta \left\| \boldsymbol{e}_d \right\|_2^2 + \eta \max \left\{ 0, \int_0^{0.5\pi} \epsilon(\gamma)^2 d\gamma - 1 \right\}, \tag{23}$$

where $\boldsymbol{\zeta}$, $\beta$ and $\eta$ are hyper-parameters related to the three penalty terms. All elements in the hyper-parameters are set to 0 during the validation and model evaluation. In general, the image sources correspond to higher-order reflections are assigned smaller penalty coefficients as angular errors are amplified with increasing number of reflections.

## III. SIMULATION STUDIES

To study the effectiveness of our proposed method, we consider four common applications of ocean acoustic propagation models. These are summarized in Fig. 6.
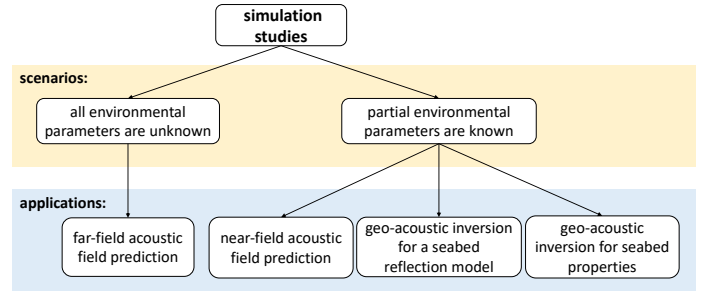


Fig. 6: Summary of the application scenarios demonstrated via simulation studies.

All four applications considered use a profiling float equipped with a single hydrophone, collecting acoustic field measurements at a constant sampling rate. Such floats provide a cost-effective way of sparsely sampling an acoustic field. We assume that the profiling float can control its motion vertically, but not horizontally. The float freely drifts horizontally with ocean currents, thus following a zig-zag trajectory as it moves up and down through the water column.

### A. Far-field acoustic field prediction

The first application we shall consider is that of acoustic field prediction within an AOI at a long distance from an acoustic source. Suppose we have acoustic measurements from a profiling float along a zig-zag trajectory through the AOI, but no other environmental knowledge. Conventional propagation models cannot be used for this application, as they require environmental knowledge as input. As discussed in Section II-B, RBNN parameters $\mathcal{T}_{\text{p}}$ can be learnt without prior environmental knowledge, with acoustic field measurements at a few points as training data. With a sufficiently large distance
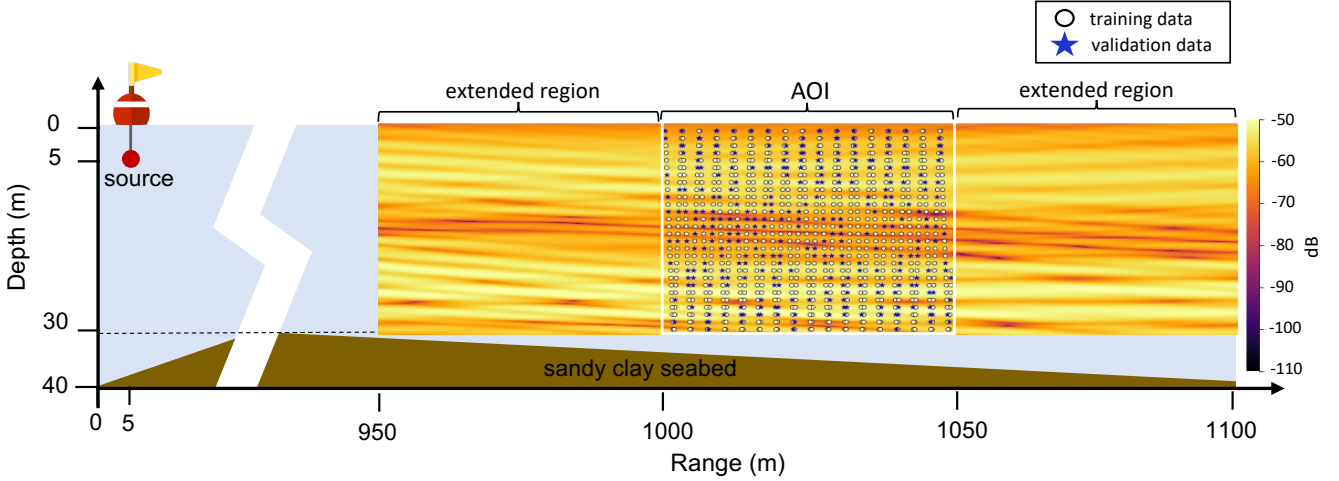
Fig. 7: Simulated environment for the far-field acoustic field prediction application. The trajectory of the profiling float can be seen in terms of the training data points. The ground truth field pattern within the AOI is also shown.

TABLE III: SIMULATED ENVIRONMENTAL SETUP FOR THE FAR-FIELD ACOUSTIC FIELD PREDICTION APPLICATION.

| Parameters | Value |
|---|---|
| Environmental model | 2D |
| Frequency | 10 kHz |
| Seabed | Sandy clay |
| Bathymetry | Range-dependent |
| Source depth | 5 m |
| Sound speed | 1,541 m/s |
| Distance between source and AOI | 995 m |
| Dimensions of AOI | 50 m × 30 m |
| Number of training data | 688 |
| Number of validation data | 296 |
| Number of test data | 601,601 |
| Number of rays in the RBNN layer | 60 |

TABLE IV: MODEL COMPLEXITY AND RMS TEST ERROR OF THE THREE MODELS FOR FIELD PREDICTIONS WITHIN THE AOI.

| Method | Model parameters | RMS test error (dB) | |
|---|---|---|---|
| | | Error-free data | Noisy data |
| RBNN[1] | 60 | 3.082 | 4.258 |
| GPR | 1374[2] | 3.211 | 3.167 |
| DNN | 6421 | 3.488 | 3.372 |

[1] Plane-wave RBNN.
[2] Dimensionality of each data point × training data size.

between the acoustic source and the AOI, the plane wave RBNN formulation may be used to approximate the acoustic propagation in the AOI.

We simulate a profiling float performing 17 profiles through a 50 m × 30 m AOI at a distance of 995 m from a 10 kHz source deployed at a depth of 5 m. The simulation setup is detailed in Table III and illustrated in Fig. 7. A total of 984 acoustic field measurements are collected along the trajectory of the float, of which 70% are used to train the RBNN model, and the remaining 30% used for validation. We wish to predict the acoustic field in the entire AOI.

We benchmark the field estimation performance of the RBNN against two popular data-driven techniques: GPR and DNN. We use a GPR with a composite kernel of a squared exponential isotropic kernel and a Matérn $5/2$ ARD kernel, as this is a common choice for multi-dimensional regression problems. The DNN model used has 3 fully-connected hidden layers with ReLU as activate function.

We use the Bellhop model [55] to generate the 984 synthetic acoustic measurements along the profiler's trajectory for training and validation. The high frequency source produces a complex interference pattern. To evaluate the field prediction performance in simulation, we generate a dense test dataset of 601,601 data points over a grid covering the AOI, with a resolution of 0.05 m in depth and range. The trainable model parameters in RBNN and DNN models are random initialized. We therefore carry out 10 Monte Carlo simulations for the RBNN and DNN models and present the results with the best validation error. The hyper-parameters in the GPR kernel are chosen to yield the best performance based on the validation data. We also add a random position error of up to 0.1 m on each dimension of the measurement locations of the training and validation data to evaluate model robustness.

The root mean square (RMS) test error and the model complexity (number of model parameters) of the three models are reported in Table IV. The acoustic field patterns estimated by the three approaches are shown in Fig. 8. All of the three methods are able to learn key features of the acoustic fields within the AOI. The RBNN model recovers most of the details in the AOI and extrapolates well in an *extended region* beyond the AOI. The GPR learns the field pattern well within the AOI where training data is available, but fails to extrapolate the field in the extended region. The field pattern reconstructed by the DNN has the lowest fidelity among the three approaches. The extrapolated field by the DNN also deviates significantly from the ground truth. The extrapolated field patterns shown in Fig. 8 (f), (g) and (h) highlight the unique ability of the
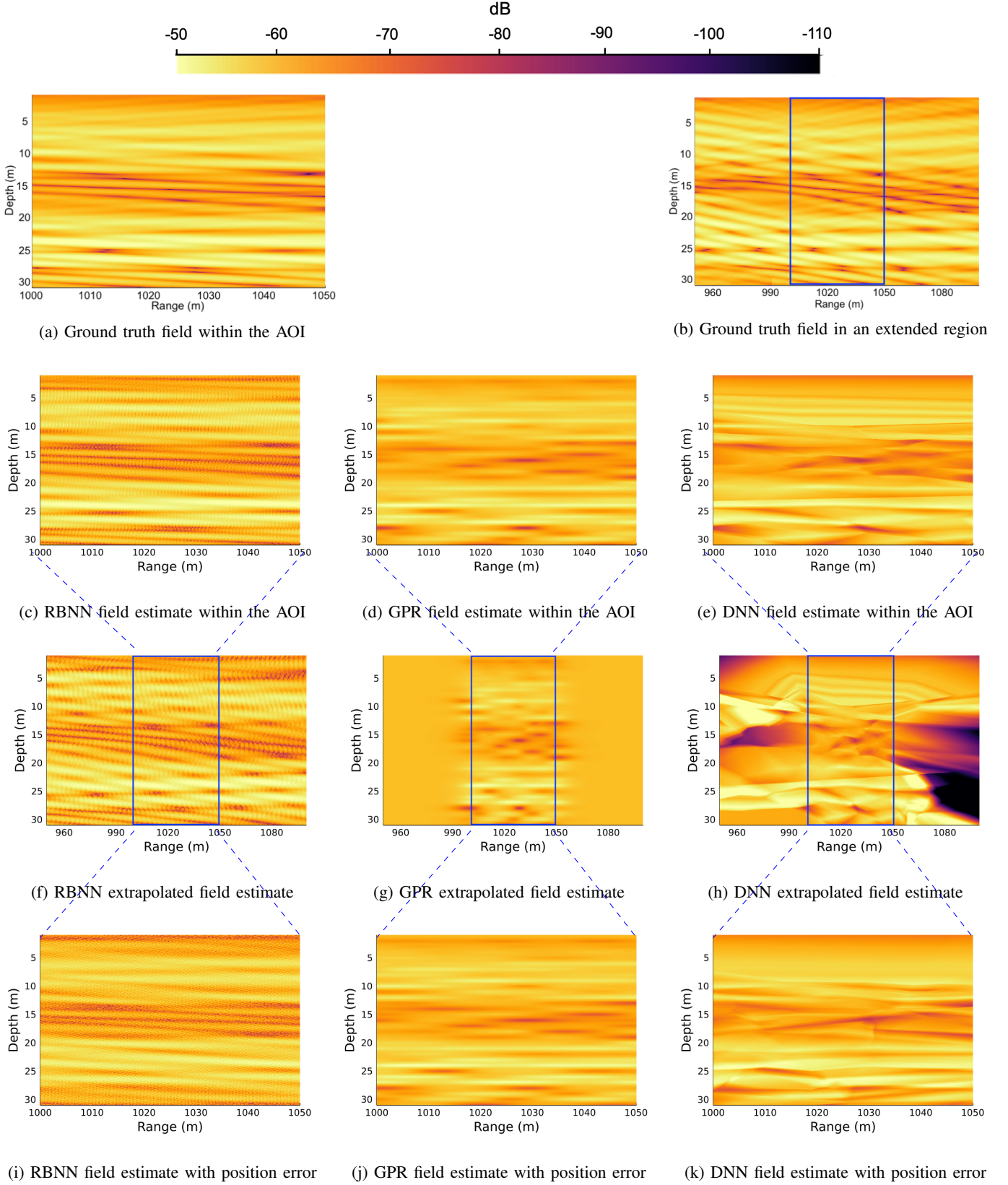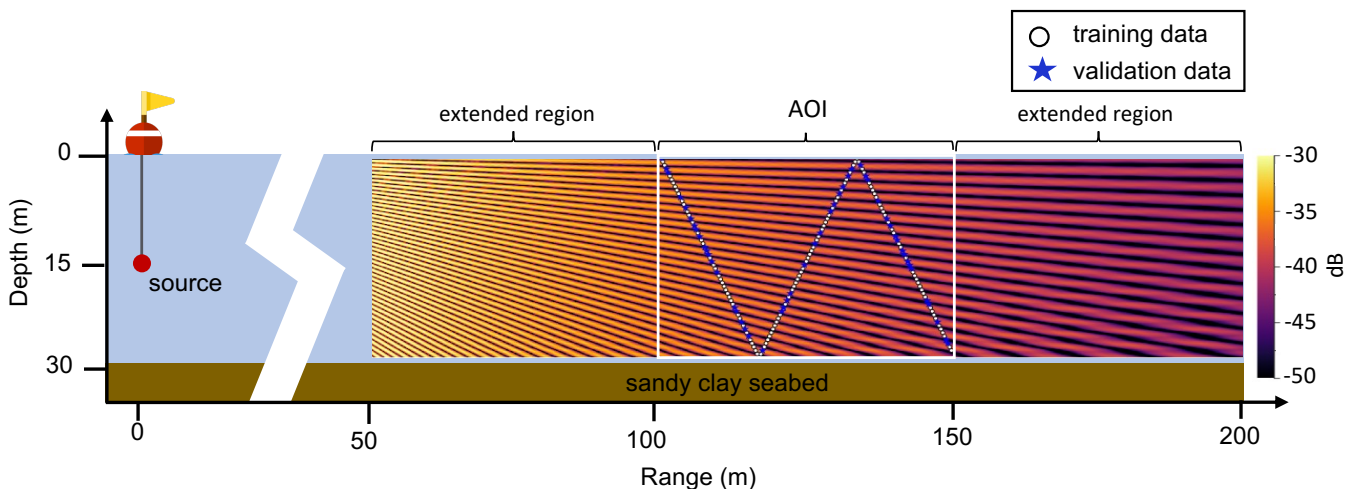
(a) Ground truth field within the AOI

(b) Ground truth field in an extended region

(c) RBNN field estimate within the AOI

(d) GPR field estimate within the AOI

(e) DNN field estimate within the AOI

(f) RBNN extrapolated field estimate

(g) GPR extrapolated field estimate

(h) DNN extrapolated field estimate

(i) RBNN field estimate with position error

(j) GPR field estimate with position error

(k) DNN field estimate with position error

Fig. 8: The estimated field patterns for the far-field acoustic field prediction application. Panel (a) shows the ground truth field pattern within the AOI, while panel (b) shows the ground truth field within a 50 m extended area on both side of the AOI. Panels (c)–(e) show the estimated fields by RBNN, GPR and DNN. Panels (f)–(h) show the corresponding extrapolated field by RBNN, GPR and DNN in the extended region. Panels (i)–(k) show the estimated field when the training data has positional errors.

Fig. 9: Simulated environment for the near-field acoustic field prediction application. The trajectory of the profiling float can be seen in terms of the training data points. The ground truth field pattern within the AOI is also shown.

RBNN to not only interpolate well, but also to extrapolate.

The field estimation performance of the GPR and the DNN, as quantified by RMS test error, is not significantly affected by position errors in the dataset. On the other hand, the field estimation accuracy of the plane wave RBNN was found to be vulnerable to position errors. Interestingly though, the qualitative field patterns seen in Fig. 8 (i), (j) and (k) show that the RBNN captures the overall field pattern best, even in the case of position errors.

### B. Near-field acoustic field prediction

We next consider an acoustic field prediction application within an AOI from a less distant source assuming that the channel geometry is known. Acoustic measurements are collected along a zig-zag trajectory within AOI using a profiling float. Since some of the environmental parameters (e.g. seabed properties) are unknown, we cannot employ conventional propagation models for field prediction. We can, however, use the spherical wave RBNN from Section II-C2 with the knowledge of channel geometry. We can calculate the nominal arrival ray directions $\theta'$, $\psi'$ and propagation distances $d'$ prior to the training. This significantly improves the training effectiveness and accuracy.

For this application, we use a simple spherical wave RBNN model based on (19), without the RCNN layer. The overall effect of the reflections and absorption is modeled with a set of trainable parameters $A$, associated with the set of rays. To model geometrical measurement errors, we also add error parameters for nominal direction and propagation distances. The set of trainable parameters therefore is:

$$\mathcal{T}_s \equiv \left(k, e_\theta, e_\psi, e_d, A, \phi\right). \tag{24}$$

The setup of the simulated environment is shown in Fig. 9 and summarized in Table V. A profiling float performs 2 profiles across a 50 m × 28 m AOI at a distance of 100 m from a 5 kHz source deployed at a depth of 15 m to collect 167 acoustic field measurements. We use 70% of the collected

| Parameters | Value |
|---|---|
| Environmental model | 3D |
| Frequency | 5 kHz |
| Seabed | Sandy clay |
| Bathymetry | Range-independent |
| Water depth | 30 m |
| Source depth | 15 m |
| Sound speed | 1,541 m/s |
| Distance between source and AOI | 100 m |
| Dimension of AOI | 50 m × 28 m × 0.1 m |
| Number of training data | 116 |
| Number of validation data | 51 |
| Number of test data | 561,561 |
| Number of rays in RBNN | 60 |

measurements to train the RBNN, and aim to estimate the acoustic field in the entire AOI. We benchmark the field estimation performance of the RBNN against GPR and DNN with the same model configurations as discussed in Section III-A.

A dense test dataset of 561,561 data points on a 0.05 m spacing grid covering the AOI is generated using Bellhop to evaluate the field prediction performance. As RBNN and DNN may be sensitive to random initialization, we carry out 10 Monte Carlo simulations for each, and present the results with the best validation error. The hyper-parameters in the GPR kernel are tuned to yield the best validation error. To evaluate model robustness, we added random measurement errors in source location (0.3 m in horizontal directions, 0.1 m in depth), measurement locations (maximum of 0.4 m in all directions) and water depth (1 m) of AOI.

The RMS test errors of the estimated fields within the AOI by the three models are shown in Table VI. The acoustic field patterns within AOI estimated by the three approaches are shown in Fig. 10 (c), (d) and (e). Fig. 10 (f), (g) and (h) show extrapolated fields by the three models. The RBNN model is
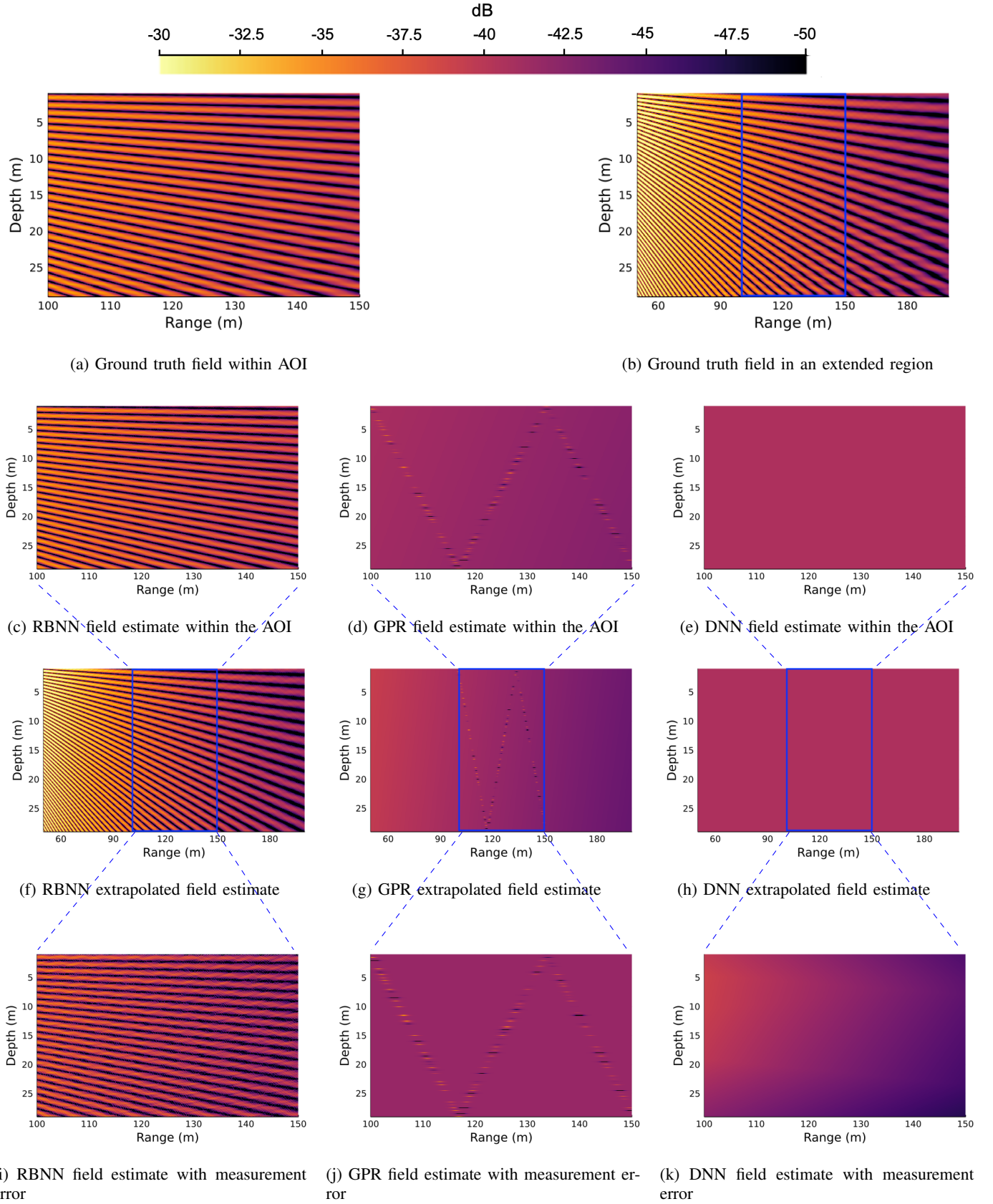
(a) Ground truth field within AOI

(b) Ground truth field in an extended region

(c) RBNN field estimate within the AOI

(d) GPR field estimate within the AOI

(e) DNN field estimate within the AOI

(f) RBNN extrapolated field estimate

(g) GPR extrapolated field estimate

(h) DNN extrapolated field estimate

(i) RBNN field estimate with measurement error

(j) GPR field estimate with measurement error

(k) DNN field estimate with measurement error

Fig. 10: The estimated field patterns for the near-field acoustic field prediction application. Panel (a) shows the ground truth field pattern within the AOI, while panel (b) shows the ground truth field within a 50 m extended area on both side of the AOI. Panels (c)–(e) show the estimated fields by RBNN, GPR and DNN. Panels (f)–(h) show the corresponding extrapolated field by RBNN, GPR and DNN in the extended region. Panels (i)–(k) show the estimated field when the position and geometry measurements have random errors.
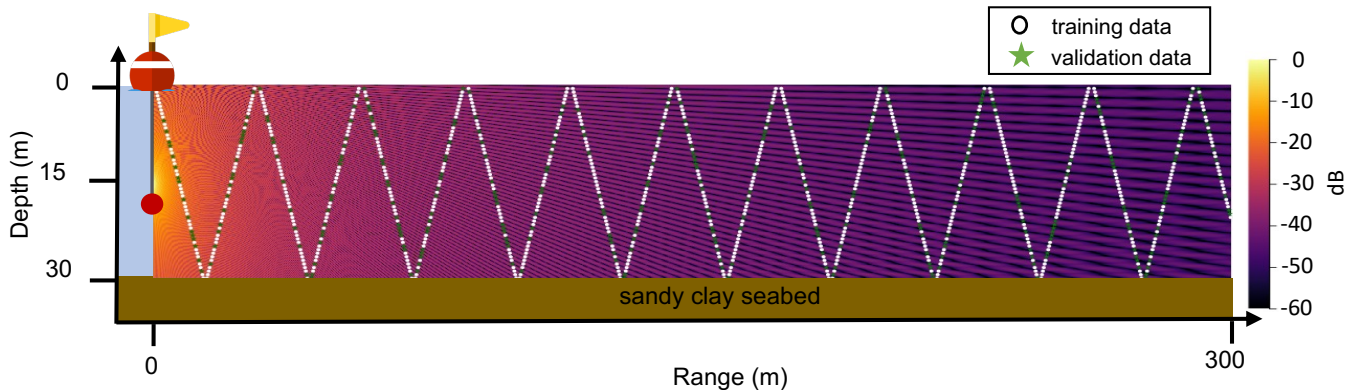
Fig. 11: Simulated environment for geo-acoustic inversion for seabed reflection model. The trajectory of the profiling float can be seen in terms of the training data points. The ground truth field pattern within the AOI is also shown.

TABLE VI: RMS TEST ERROR FOR THE NEAR-FIELD ACOUSTIC FIELD PREDICTION APPLICATION.

| Method | RMS test error (dB) | |
|---|---|---|
| | Error-free data | Noisy data |
| RBNN | 1.688 | 6.519 |
| GPR | 7.011 | 7.056 |
| DNN | 7.118 | 7.142 |

TABLE VII: SENSITIVITY OF RMS TEST ERROR OF FIELD ESTIMATION TO RANDOM POSITION ERROR, FOR THE NEAR-FIELD ACOUSTIC FIELD PREDICTION APPLICATION.

| Maximum position error[1] (m) | RMS test error (dB) |
|---|---|
| 0.0 | 1.688 |
| $0.1\sqrt{3}$ | 3.696 |
| $0.2\sqrt{3}$ | 4.900 |
| $0.3\sqrt{3}$ | 5.139 |
| $0.4\sqrt{3}$ | 6.519 |

[1] Maximum position error per dimension $\times\sqrt{3}$.

able to predict and extrapolate the spatially fast-varying field patterns well, even with a much smaller training data set as compared to the far-field acoustic field prediction application in the previous section. However, the GPR and DNN show poor performance in terms of the estimated field pattern and RMS test error, for both interpolation and extrapolation of the acoustic field. The results highlight that the data-efficiency of the RBNN model – the model can effectively incorporate knowledge of channel geometry and therefore train with very little data. The conventional GPR and DNN models, on the other hand, fail to predict field patterns as they do not benefit from the partial environmental knowledge.

As one would expect, measurement noise worsens the prediction accuracy for the RBNN model. The sensitivity of field estimation to position errors is summarized in Table VII. However, the qualitative field pattern can still be recovered even with large measurement errors as seen in Fig. 10 (i).

### C. Geo-acoustic inversion for a seabed reflection model

The third application we demonstrate is to extract a seabed reflection model from acoustic measurements. Seabed reflection depends on the seabed structure and material properties, which are often unknown. In applications where multipath arrivals overlap and cannot be separated, we cannot measure the reflection coefficient directly. Our proposed recipe can, however, learn a reflection model from observed total transmission loss at a number of observation points. We use the RBNN model from Section II-C2 together with the RCNN layer, where the RCNN models the unknown reflection coefficient (as a function of reflection angle). By training the composite spherical wave model described in (19), we can recover a trained RCNN as a model for the seabed reflection.
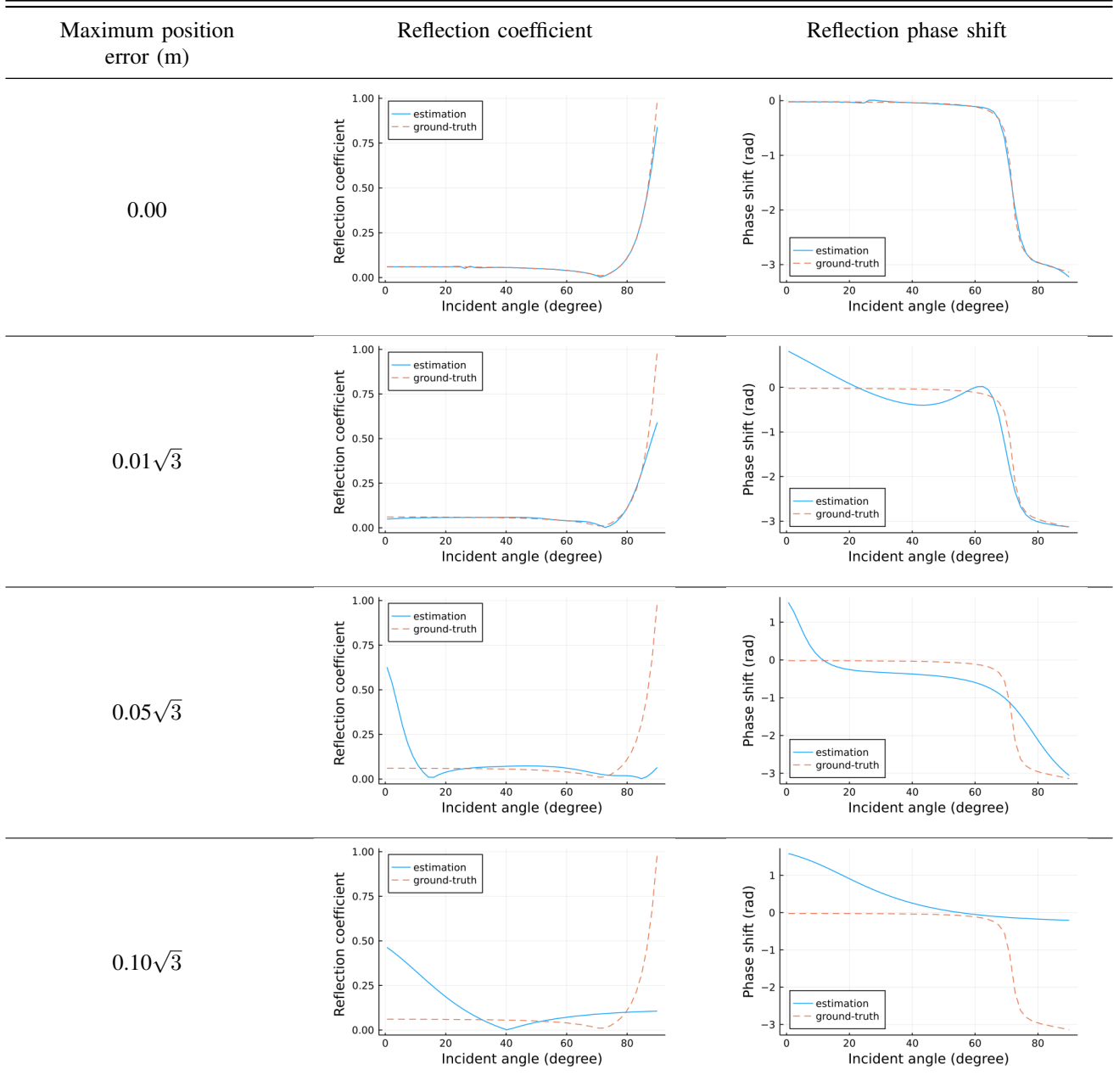
We assume that the channel geometry and source location are known. A profiling float is employed to perform 10 profiles through a 300 m × 30 m AOI from a 5 kHz source deployed at a depth of 15 m. The simulation setup is illustrated in Fig. 11. A total of 1,150 acoustic field measurements are collected along the trajectory, and 70% of them are used to train the composite RBNN model. The environmental setup is similar to the near-field acoustic field prediction application in Section III-B, and the synthetic data is generated using Bellhop. We pre-calculate the nominal arrival directions and propagation distances and use acoustic data to optimize the trainable model parameters $\mathcal{T}_{sg}$ given in (22).

In Table VIII, we present the inferred reflection coefficient curves and phase shift curves for various amount of position measurement error. In an ideal scenario with no measurement errors, we can accurately recover the seabed reflection model. The modeling errors increase with the amount of position measurement error, as one would expect. The effect of measurement error can be partially mitigated by increasing the size of the training dataset.

### D. Geo-acoustic inversion for seabed properties

The last application we shall consider is a geo-acoustic inversion problem, where we wish to determine geo-acoustic seabed properties from acoustical field measurements. We consider a simple Rayleigh reflection model to illustrate the

TABLE VIII: Effect of measurement position error on the seabed reflection model.

| Maximum position error (m) | Reflection coefficient | Reflection phase shift |
| --- | --- | --- |
| 0.00 | | |
| $0.01\sqrt{3}$ | | |
| $0.05\sqrt{3}$ | | |
| $0.10\sqrt{3}$ | | |



idea. The complex Rayleigh reflection coefficient is given by [53]:

$$\Gamma = \frac{\rho_r \cos\gamma - \sqrt{(\frac{\bar{\delta}}{c_r})^2 - \sin\gamma^2}}{\rho_r \cos\gamma + \sqrt{(\frac{\bar{\delta}}{c_r})^2 - \sin\gamma^2}}, \quad (25)$$

where

$$\bar{\delta} = 1 + i\delta, \quad (26a)$$

$$\rho_r = \frac{\rho_{\text{seabed}}}{\rho_{\text{seawater}}}, \quad (26b)$$

$$c_r = \frac{c_{\text{seabed}}}{c_{\text{seawater}}}, \quad (26c)$$

where $\delta$ denotes dimensionless seabed absorption coefficient, $\rho_r$ denotes relative density, $c_r$ represents relative sound speed.

We assume $\rho_r$, $c_r$ and $\delta$ are unknown and to be determined from acoustic field measurements.

We assume that the source and receiver locations, as well as the channel geometry are known. An acoustic float is employed to take 166 acoustic measurements over 100 m × 30 m AOI along a zig-zag trajectory from a 5 kHz acoustic source deployed at a depth of 15 m. As in previous applications, 70% of the measurements are used to train the RBNN model, while the balance 30% is used for validation. Fig. 12 depicts the simulated environment and the sampling trajectory of the acoustic float.

In Section III-C, we modeled the angle-dependent complex reflection coefficient using a RCNN. While this is useful for acoustic propagation modeling, this approach does not yield
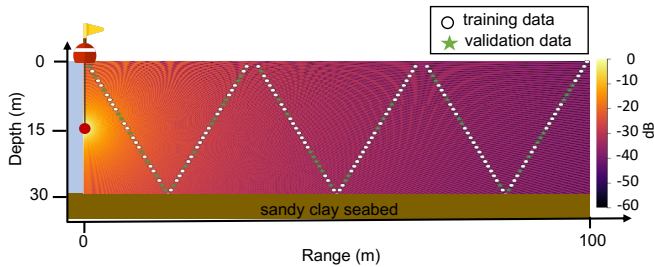
Fig. 12: Simulated environment for the geo-acoustic inversion of seabed properties. The trajectory of the profiling float can be seen in terms of the training data points. The ground truth field pattern within the AOI is also shown.

TABLE IX: Estimated seabed parameters as a function of maximum position measurement error.

| Maximum error (m) | Training dataset | $\rho_r$ [% error] | $c_r$ [% error] | $\log(\delta)$ (dB) [% error] |
|---|---|---|---|---|
| 0.00 | 166 | 1.147 [0.0%] | 0.985 [0.0%] | -2.616 [0.0%] |
| $0.01\sqrt{3}$ | 166 | 1.221 [1.2%] | 0.998 [-0.7%] | -2.910 [-11.2%] |
| $0.05\sqrt{3}$ | 252 | 1.055 [-8.0%] | 0.988 [0.3%] | -2.222 [15.1%] |
| $0.10\sqrt{3}$ | 335 | 1.153 [0.5%] | 0.994 [0.9%] | -3.810 [-45.6%] |
| $0.20\sqrt{3}$ | 335 | 1.204 [5.0%] | 0.948 [-3.7%] | -3.342 [-27.8%] |
| $0.50\sqrt{3}$ | 421 | 1.257 [8.1%] | 0.992 [0.8%] | -4.211 [-61.0%] |

estimates of geo-acoustic properties such as $\rho_r$, $c_r$ and $\delta$. We therefore replace the RCNN layer in (19) with the expression for complex reflection coefficient from (25), and train the resultant composite RBNN. The set of trainable parameters for this RBNN is:

$$\mathcal{T}_{sg} \equiv (k, \boldsymbol{e}_\theta, \boldsymbol{e}_\psi, \boldsymbol{e}_d, \rho_r, c_r, \delta). \tag{27}$$

Table IX summarizes the estimated values and percentage error for the three unknown geo-acoustic parameters for various levels of position measurement errors. With accurate measurements, the model is effective in accurately determining the geo-acoustic parameters. In the presence of position errors, we need to increase the training data size to improve model robustness. The robustness of geo-acoustic inversion depends on the sensitivity of the acoustic field to each geo-acoustic parameter. In this example, $\rho_r$ and $c_r$ affect the acoustic field more strongly than $\delta$. Increasing training dataset size improves the robustness of the estimates of $\rho_r$ and $c_r$, but much less so for $\delta$.

## IV. Experimental Validation

To further validate the acoustic field estimation performance of the proposed framework, we undertake a controlled experiment in a water tank. This allows us to make careful repeatable measurements to validate the method – something that is very difficult to do at sea due to time-variability.

The tank environment is strongly reverberant and surprisingly complicated to model. While acoustic rays in the rectangular geometry can be modeled with a 3D ray-tracer, multiple reflections lead to strong sensitivity to minor geometrical irregularities of the tank wall. The tank walls are made of an unhomogeneous composite material (fiber glass) with complicated reflection properties. This provides us a challenging acoustic propagation modeling problem to demonstrate our proposed method.

Before undertaking experimental validation, we developed a simplified simulation model of the tank to establish feasibility of applying our method to the tank environment. The simulation results are presented in Section IV-A. Once we had established feasibility and developed an understanding of what performance we might expect, we undertook experimental validation in the tank. The results from the experiment are presented in Section IV-B.

### A. Feasibility study

We simulate a 3D water tank environment with the dimension of 2.5 m × 1.2 m × 0.8 m and a 10 kHz CW signal source, as illustrated in Fig. 13. A 0.36 m × 0.9 m × 0.44 m AOI is located 0.5 m from source. The sound speed is assumed to be 1,505 m/s, in accordance with conductivity and temperature measurements in our tank. We split the AOI vertically into a training region and a test region. The training and validation data (250 and 28 data points respectively) are obtained from the training region, whereas the test region is used to test (222 data points) how well the model extrapolates beyond the training region. We adopt the spherical wave formulation with the knowledge of geometry based on (19) and (22) to predict the field in AOI. The loss function we minimize is (23).

We adopt a geometrical ray model to simulate the acoustic propagation in the tank environment, and generate synthetic acoustic measurements* within the AOI. We assume the water-air interface to be a perfect reflector with a reflection coefficient of $-1$. We adopt a simple tank sidewalls and bottom reflection model, and assume the reflection coefficient to be given by (25), with $\rho_r = 1.5$, $c_r = 0.9$ and $\delta = 0.0$. For benchmarking, we use GPR and DNN similar to those described in Section III-A. We generate a dense test dataset of 30,303 points over the entire AOI with a resolution of 0.01 m in range and width, and 0.05 m in depth. It is not practical to collect such a dense dataset during the later experiment, and so we also generate a sparse test dataset of 222 points in the test region for later benchmarking of the experimental results.

Since the measurement accuracy of tank dimensions and transducer locations in the tank is limited, we introduce measurement errors in the tank size, source location and measurement locations in simulation too. The simulated tank

*The acoustic measurements are shown in Volts, as we measure the pre-amplified output from the hydrophones in Volts during the experiment. These can be converted to $\mu$Pa by multiplying by the gain-corrected acoustic sensitivity of the hydrophone.
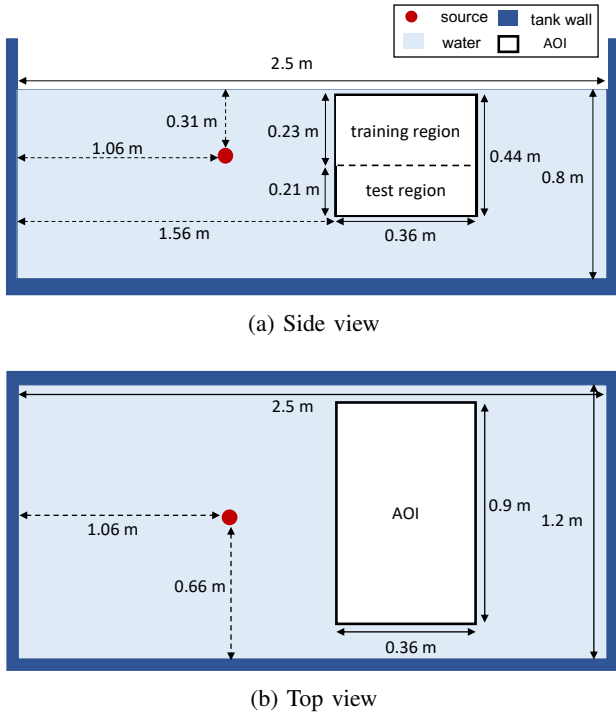
(a) Side view



(b) Top view

Fig. 13: Tank experiment setup.

TABLE X: MATE OF THE ESTIMATED ACOUSTIC FIELD FOR THE FEASIBILITY STUDY.

| Method | MATE ($V_{pp}$) | |
| --- | --- | --- |
| | Sparse | Dense |
| RBNN | 0.014 | 0.242 |
| GPR | 2.676 | 1.860 |
| DNN | 1.444 | 1.132 |

dimensions are mismatched from the geometrical knowledge available to our algorithm by 0.010 m, 0.015 m and 0.020 m in the three dimensions. The source location deviates by 0.02 m in from the location provided to the algorithm. Due to practical considerations, the measurement errors in shallower hydrophone locations in our tank is expected to be less than that for deeper locations. We therefore introduce a random error of up to 0.02 m per dimension for acoustic measurements with depths shallower than 0.36 m, and 0.04 m per dimension for deeper locations. We calculate the nominal incoming ray directions and propagation distances prior to the training. We allow our RBNN model to train the error to the nominal directions and propagation distances to cope with the erroneous source location and tank size measurements, as discussed in Section II-C2. To allow for a few measurement outliers during the experiment, we opt to minimize the mean absolute error in the training process, rather than the RMS error. This encourages the model to focus on fitting the majority of the training data well, and ignore a few outliers.

The rich multipath in the simulated water tank environment yields a complicated field pattern. Cross-sections of the ground truth field and the estimated field at four different depths within the AOI are shown in Fig. 14. Do note that the estimated

field at the depth of 0.45 m is extrapolated as none of the training data or validation data falls in this test region. We see that the RBNN model can recover and extrapolate the field reasonably well, whereas the GPR and RBNN methods fail to do so. The mean absolute test error (MATE) of the sparse and dense test datasets is shown in Table X. The sparse test error and dense test error are based on the error-free measurements. The two types of test errors are in similar range for all of the three models. This suggests that the sparse test error is a representable measure of field estimation performance. We also extrapolate the field to the entire water tank environment as shown in Fig. 15. Not surprisingly, the classical data-driven techniques fail to extrapolate the field in the region away from the AOI, whereas the RBNN model can generalize well and predict the field in the entire water tank.

### B. Controlled experiment

With the feasibility established via simulation, we carried out an experimental validation in a water tank using the same setup described in Section IV-A. The equipment setup used in the experiment is shown in Fig. 16. We used a National Instruments Data Acquisition (NI-DAQ) system to transmit a CW signal at 10 kHz with an amplitude of 1 $V_{pp}$. A pair of TC4013 acoustic transducers were used as the transmitter and receiver. 500 acoustic measurements were collected at the same locations as the data generated in the feasibility study. Each acoustic transducer was attached to a fishing line, with a reel and sliding block mechanism to to control the 3D position of the transducer as shown in Fig. 17. The water tank was located outdoors and experienced light breeze on occasion. This led to slight measurement errors due to small scale oscillations of the source and receiver. The oscillations manifest themselves as fluctuations in the amplitude and phase of the recorded signal. We computed the average envelope over a 40 second period to reduce the impact of oscillations on the measurement. The RBNN model allows for error in direction of arrival to be estimated during training.

In addition to angular errors, we also expect some errors (few cm) in measurement of location of the transducers. We design a two-stage training strategy to deal with such location measurement errors. The first stage aims to optimize the trainable parameters $\mathcal{T}$, specified in the designed RBNN model, using measured location data. We freeze the trained RBNN model at the end of this stage, and focus on estimating measurement errors in the second stage. We feed the corrected locations (measured locations offset by the estimated location errors in all dimensions) into the RBNN model to predict acoustic fields in this stage. A $L_2$-norm penalty term of absolute position errors is added in the loss function to constrain the range of position errors. By minimizing the loss function, the second stage aims to estimate the most appropriate location errors using the RBNN model parameterized by the parameters trained in the first training stage.

To benchmark the RBNN performance, we use a GPR and

(a) Ground truth field within the AOI

(b) RBNN field estimates within AOI

(c) GPR field estimates within AOI
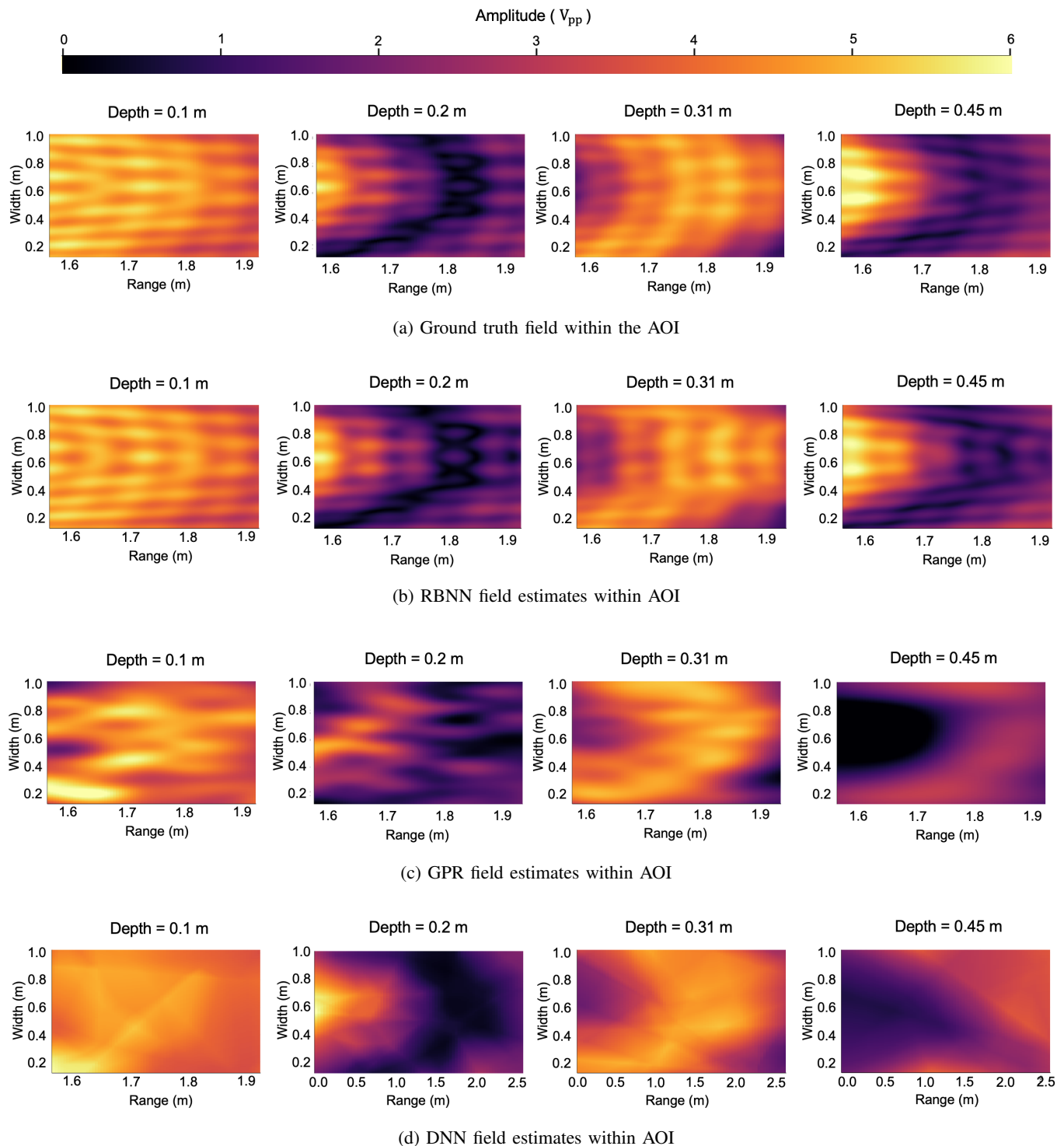
(d) DNN field estimates within AOI

Fig. 14: Ground truth and estimated acoustic field at four different depths. The depth of 0.45 m is in the test region, where no training data was made available to the three models. The other three depths are in the training region.
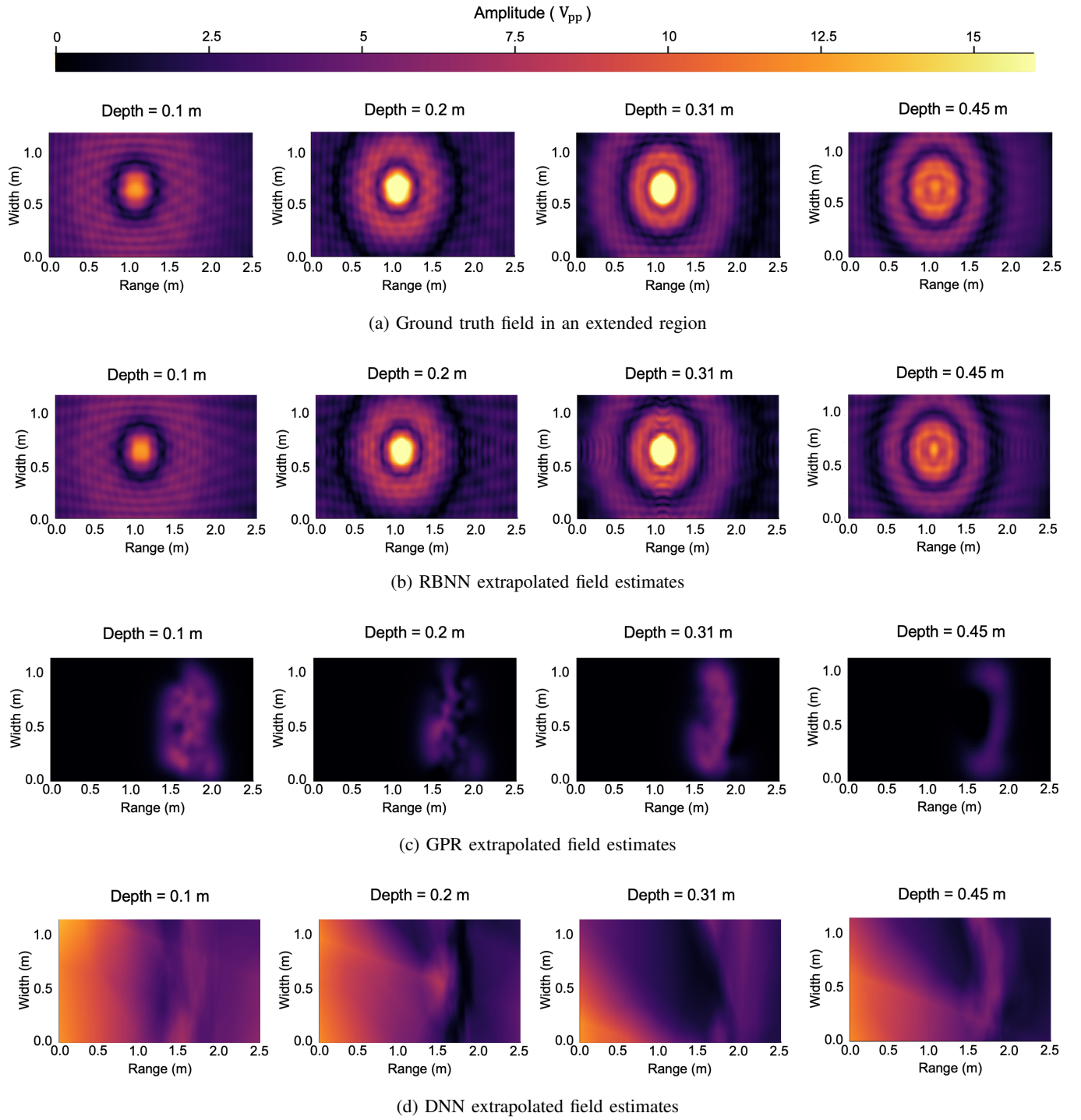
(a) Ground truth field in an extended region

(b) RBNN extrapolated field estimates

(c) GPR extrapolated field estimates

(d) DNN extrapolated field estimates

Fig. 15: Ground truth and extrapolated field within the entire tank at four different depths.
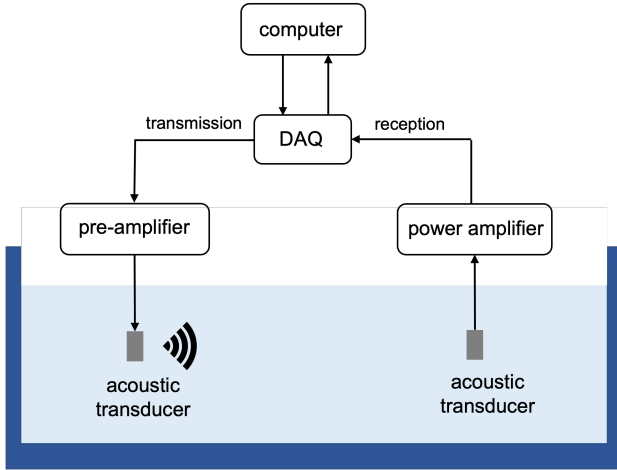
Fig. 16: Equipment setup for the controlled experiment.



Fig. 17: Water tank used for the controlled experiment.

DNN[†] as in the feasibility study. For each of the three methods, Figs. 19 and 20 show the estimated fields within the AOI and the extrapolated fields in the entire tank respectively. The field pattern extrapolated by the RBNN model looks reasonable in the sense that the region with the strongest pressure amplitude is consistent with the source location. The GPR and DNN fail to reconstruct any discernable field pattern in the tank. In line with this, the MATE of the RBNN model is significantly lower than that of the GPR and DNN models, as shown in Table XI. The absolute trained position errors for the 222 sparse test data points are shown in Fig. 18. Most errors are below 4 cm, as we would expect from our measurement procedure.

Fig. 21 shows the learnt reflection coefficient and phase shift for the water tank walls. While we do not have ground truth to validate the reflection coefficient curves, the learnt model works well to estimate the acoustic field in the tank. We observe this in the good agreement between RBNN prediction and measured data in Fig. 22, and also as a Spearman's correlation coefficient of 0.971 between the prediction and data in Table XI. On the other hand, the GPR and DNN simply learn to predict average values regardless of the measurement

---

[†]We found that the DNN performed better with experimental data if we replaced the ReLU activation function with a hyperbolic tangent (tanh) activation function, and therefore we present results for the tanh-activated DNN in this section.

TABLE XI: PERFORMANCE EVALUATION OF THE ESTIMATED ACOUSTIC FIELD FROM THE CONTROLLED EXPERIMENT.

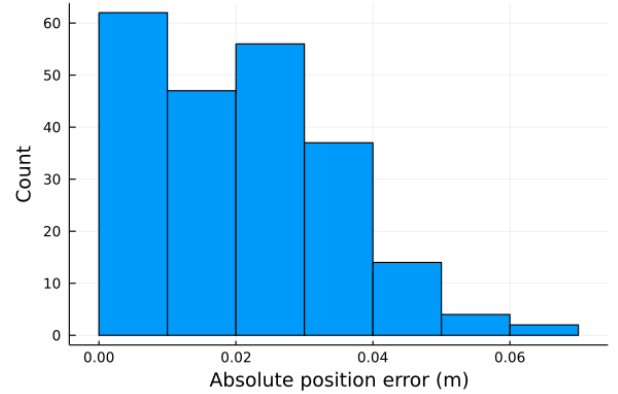| Method | MATE ($V_{pp}$) | MATE (dB) | Spearman's correlation coefficient |
|---|---|---|---|
| RBNN | 0.003 | 0.381 | 0.971 |
| GPR | 0.021 | 3.675 | -0.064 |
| DNN | 0.024 | 4.147 | -0.139 |



Fig. 18: Trained absolute position error of the sparse test data using the RBNN model.

location. The results obtained from the controlled experiment thus validate the efficacy of our proposed method to model acoustic propagation in unknown or partially known environments.

## V. DISCUSSION & CONCLUSIONS

The RBNN framework offers a high-frequency physics-based acoustic propagation modeling approach that can incorporate known environmental information and be trained with observed data, making it suitable for solving inverse problems in acoustics with limited data. The approach that we took to derive the RBNN from a high-frequency approximation to the solution of a wave equation can also be applied to other approximations. For example, applying the same approach to a normal mode approximation may yield normal-mode neural networks that may be used for low-frequency acoustic propagation problems.

We demonstrated a few applications of the RBNN framework, highlighting the flexibility it provides in modeling acoustic propagation scenarios with varying degrees of environmental complexity and knowledge. We believe that the framework can be applied to solve a much wider variety of acoustic propagation problems, especially inverse and data-aided problems. The RBNN framework can easily incorporate environmental complexities such as range-dependent bathymetry, non-isovelocity sound speed profiles, and various geo-acoustic models. When the physics is fully or partially known, explicit expressions can be included in the computational graph, with potentially some unknown parameters. On the other hand, when physics is unknown, neural networks can be used as components of the computational graph to

(a) RBNN field estimates within AOI



(b) GPR field estimates within AOI
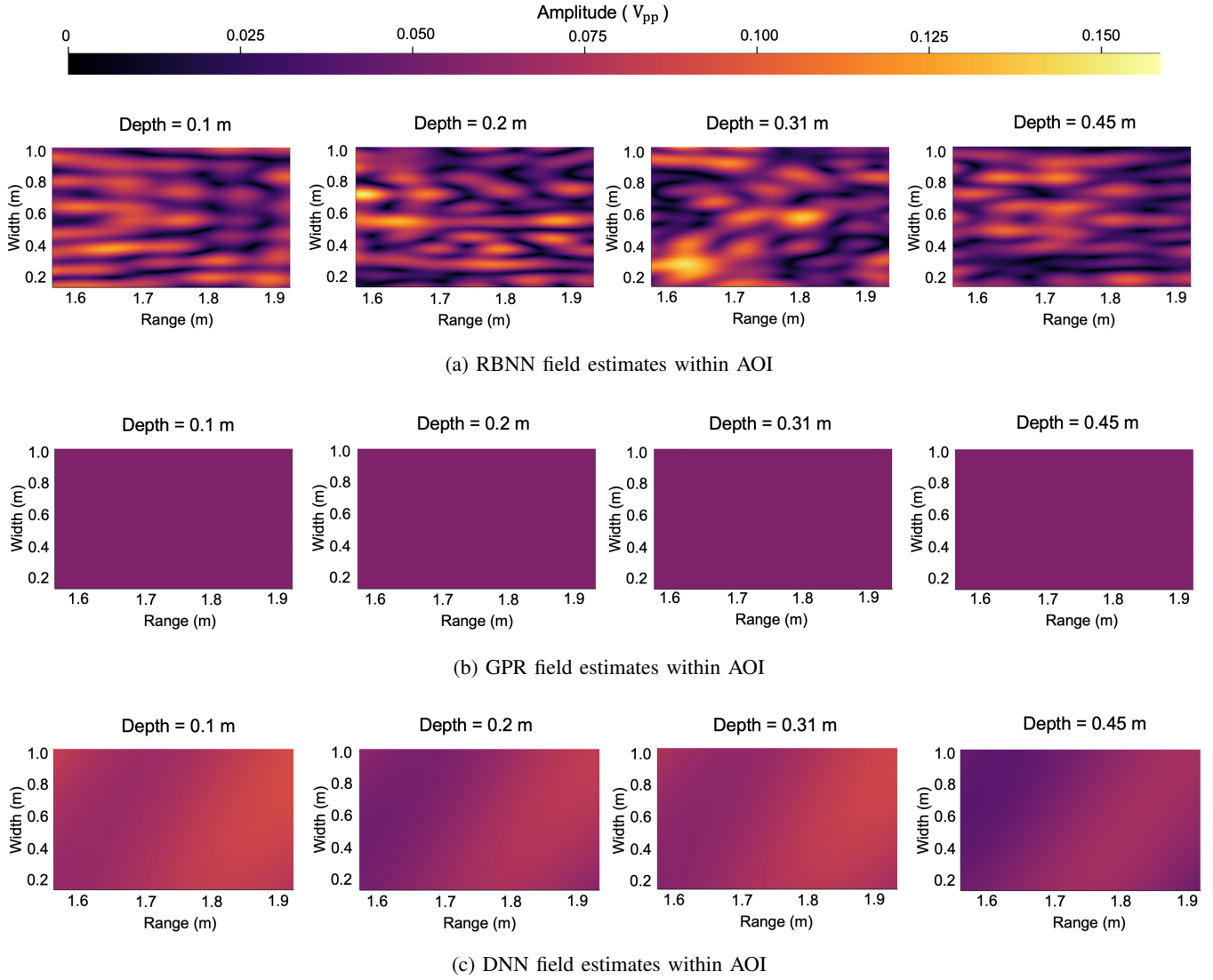


(c) DNN field estimates within AOI

Fig. 19: Estimated field patterns within AOI using the experimental data by the three models.

model arbitrary functions. The resulting computational graph can be automatically differentiated with respect to the model parameters, thus making it suitable for training with standard gradient-descent based neural network training algorithms such as ADAM.

While classical machine learning techniques such as GPR and DNN can also use data to approximate an unknown acoustic propagation model, they lack the ability to incorporate scientific domain knowledge (in our case, the acoustic wave equation) and environmental knowledge (e.g. known channel geometry). Without incorporating the domain or environmental knowledge, these techniques tend to be data-hungry during training, and extrapolate poorly. They can also make predictions that are physically unrealistic. On the other hand, we showed that the RBNN-based methods can learn from very little data, extrapolate well beyond the region where training data is available, and always make predictions that are consistent with physics.

REFERENCES

[1] L. Wang, K. Heaney, T. Pangerc, P. Theobald, S. Robinson, and M. Ainslie, "Review of underwater acoustic propagation models.," tech. rep., National Physical Laboratory, 2014.

[2] K. R. James and D. R. Dowling, "A method for approximating acoustic-field-amplitude uncertainty caused by environmental uncertainties," *The Journal of the Acoustical Society of America*, vol. 124, no. 3, pp. 1465–1476, 2008.

[3] S. Gul, S. S. H. Zaidi, R. Khan, and A. B. Wala, "Underwater acoustic channel modeling using bellhop ray tracing method," in *2017 14th International Bhurban Conference on Applied Sciences and Technology (IBCAST)*, pp. 665–670, IEEE, 2017.

[4] J. Llor and M. P. Malumbres, "Underwater wireless sensor networks: how do acoustic propagation models impact the performance of higher-level protocols?," *Sensors*, vol. 12, no. 2, pp. 1312–1335, 2012.

[5] N. R. Chapman, *Inverse Problems in Underwater Acoustics*, pp. 1723–1735. New York, NY: Springer New York, 2008.

[6] N. R. Chapman, S. Chin-Bing, D. King, and R. B. Evans, "Benchmark-ing geoacoustic inversion methods for range-dependent waveguides," *IEEE journal of oceanic engineering*, vol. 28, no. 3, pp. 320–330, 2003.

[7] S. Dosso, M. Yeremy, J. Ozard, and N. Chapman, "Estimation of ocean-bottom properties by matched-field inversion of acoustic field data," *IEEE Journal of Oceanic Engineering*, vol. 18, no. 3, pp. 232–239, 1993.
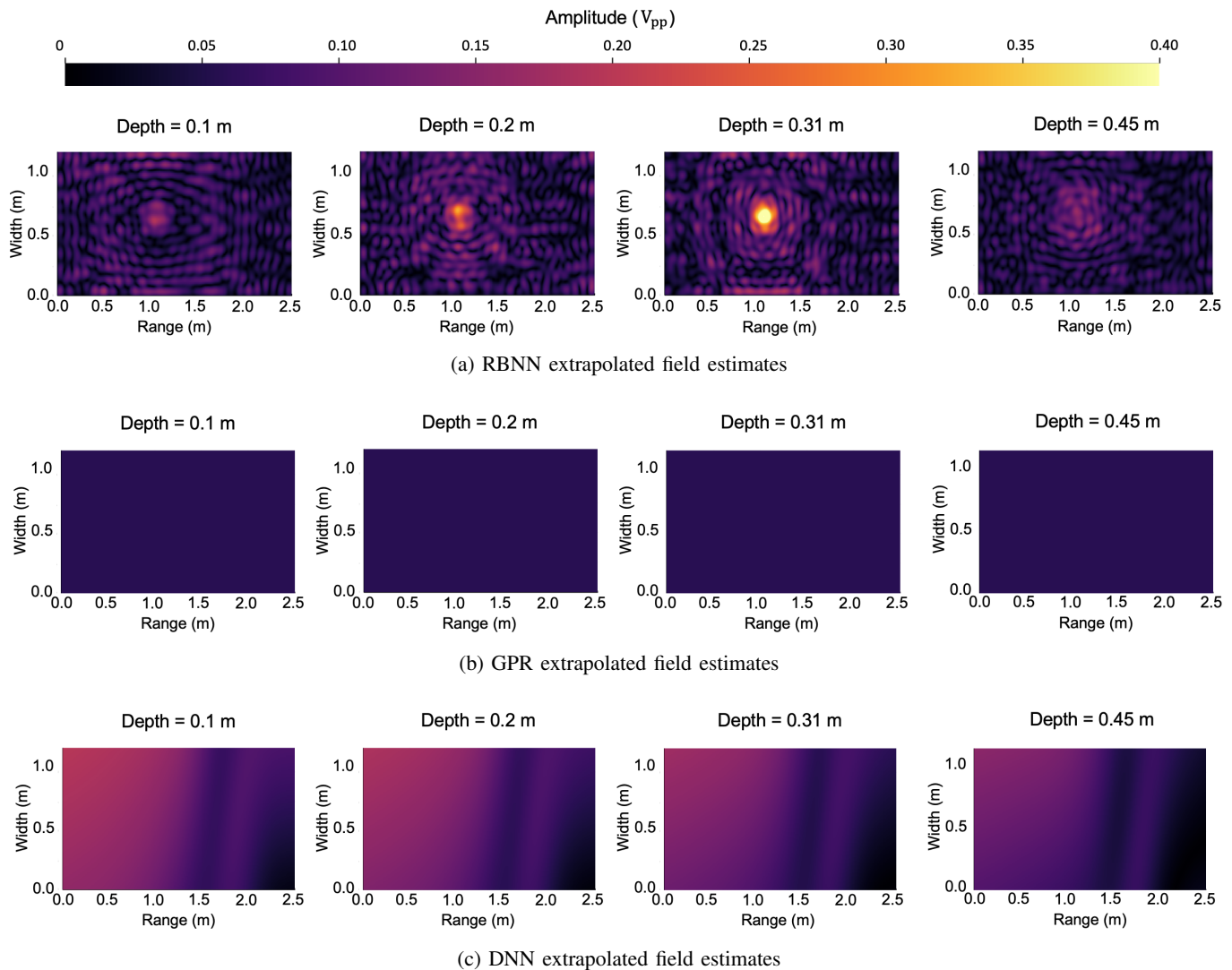
(a) RBNN extrapolated field estimates



(b) GPR extrapolated field estimates



(c) DNN extrapolated field estimates

Fig. 20: Extrapolated field patterns of the entire tank environment using the experimental data by the three models.

[8] J. Bonnel, B. Nicolas, J. I. Mars, and S. C. Walker, "Estimation of modal group velocities with a single receiver for geoacoustic inversion in shallow water," *The Journal of the Acoustical Society of America*, vol. 128, no. 2, pp. 719–727, 2010.

[9] M. Collins and W. Kuperman, "Inverse problems in ocean acoustics," *Inverse Problems*, vol. 10, no. 5, p. 1023, 1994.

[10] A. Tolstoy, "Applications of matched-field processing to inverse problems in underwater acoustics," *Inverse Problems*, vol. 16, no. 6, p. 1655, 2000.

[11] A. B. Baggeroer, W. Kuperman, and H. Schmidt, "Matched field processing: Source localization in correlated noise as an optimum parameter estimation problem," *The Journal of the Acoustical Society of America*, vol. 83, no. 2, pp. 571–587, 1988.

[12] A. B. Baggeroer, W. A. Kuperman, and P. N. Mikhalevsky, "An overview of matched field methods in ocean acoustics," *IEEE Journal of Oceanic Engineering*, vol. 18, no. 4, pp. 401–424, 1993.

[13] F. B. Jensen, W. A. Kuperman, M. B. Porter, and H. Schmidt, *Wave Propagation Theory*, pp. 65–153. New York, NY: Springer New York, 2011.

[14] T. C. A. Oliveira, Y.-T. Lin, and M. B. Porter, "Underwater sound propagation modeling in a complex shallow water environment," *Frontiers in Marine Science*, vol. 8, p. 1464, 2021.

[15] F. B. Jensen, W. A. Kuperman, M. B. Porter, and H. Schmidt, *Ray Methods*, pp. 155–232. New York, NY: Springer New York, 2011.

[16] F. B. Jensen, W. A. Kuperman, M. B. Porter, and H. Schmidt, *Normal Modes*, pp. 337–455. New York, NY: Springer New York, 2011.

[17] F. B. Jensen, W. A. Kuperman, M. B. Porter, and H. Schmidt, *Parabolic Equations*, pp. 457–529. New York, NY: Springer New York, 2011.

[18] F. B. Jensen, W. A. Kuperman, M. B. Porter, and H. Schmidt, *Wavenumber Integration Techniques*, pp. 233–335. New York, NY: Springer New York, 2011.

[19] A. Tolstoy, "3-d propagation issues and models," *Journal of Computational Acoustics*, vol. 4, no. 03, pp. 243–271, 1996.

[20] J. T. Etgen and M. J. O'Brien, "Computational methods for large-scale 3d acoustic finite-difference modeling: A tutorial," *Geophysics*, vol. 72, no. 5, pp. SM223–SM230, 2007.

[21] W. Liu, L. Zhang, W. Wang, Y. Wang, S. Ma, X. Cheng, and W. Xiao, "A three-dimensional finite difference model for ocean acoustic propagation and benchmarking for topographic effects," *The Journal of the Acoustical Society of America*, vol. 150, no. 2, pp. 1140–1156, 2021.

[22] M. S. Ballard, "Three-dimensional acoustic propagation under a rough sea surface," in *Proceedings of Meetings on Acoustics ICA2013*, vol. 19, Acoustical Society of America, 2013.

[23] P. R. Williamson and R. G. Pratt, "A critical review of acoustic wave modeling procedures in 2.5 dimensions," *Geophysics*, vol. 60, no. 2, pp. 591–595, 1995.

[24] D. B. Reeder, L. Y. Chiu, and C.-F. Chen, "Experimental evidence of horizontal refraction by nonlinear internal waves of elevation in shallow water in the south china sea: 3d versus nx2d acoustic propagation
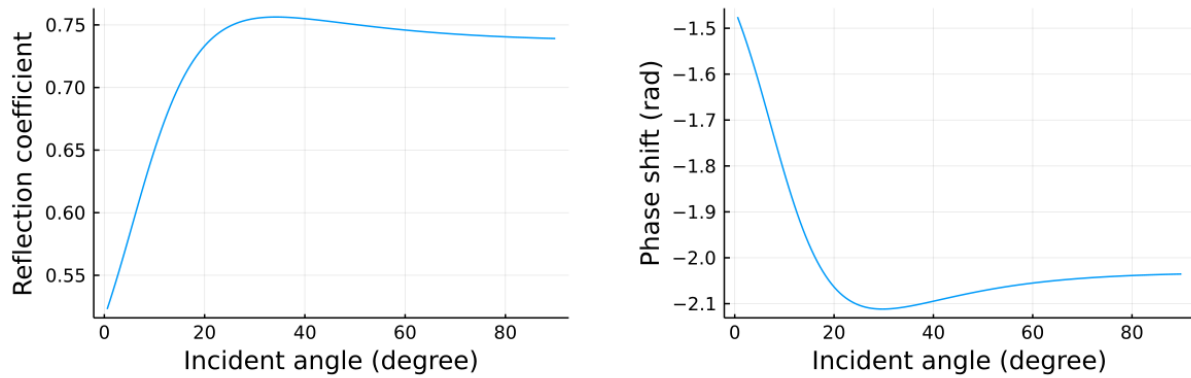
Fig. 21: Estimated reflection model based on the trained RCNN layer of the composite RBNN.
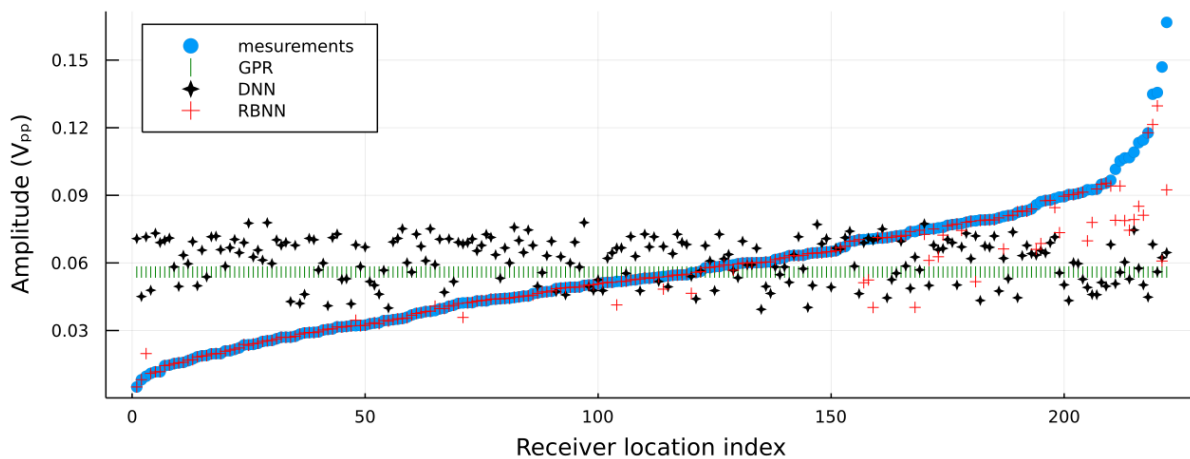


Fig. 22: Comparison between test data and model predictions.

modeling," *Journal of Computational Acoustics*, vol. 18, no. 03, pp. 267–278, 2010.

[25] M. I. Jordan and T. M. Mitchell, "Machine learning: Trends, perspectives, and prospects," *Science*, vol. 349, no. 6245, pp. 255–260, 2015.

[26] I. Goodfellow, Y. Bengio, and A. Courville, "Machine learning basics," *Deep learning*, vol. 1, no. 7, pp. 98–164, 2016.

[27] H. Yang, K. Lee, Y. Choo, and K. Kim, "Underwater acoustic research trends with machine learning: general background," *Journal of Ocean Engineering and Technology*, vol. 34, no. 2, pp. 147–154, 2020.

[28] J. Bernardo, J. Berger, A. Dawid, A. Smith, *et al.*, "Regression and classification using gaussian process priors," *Bayesian statistics*, vol. 6, p. 475, 1998.

[29] H. Liu, Y.-S. Ong, X. Shen, and J. Cai, "When gaussian process meets big data: A review of scalable gps," *IEEE transactions on neural networks and learning systems*, vol. 31, no. 11, pp. 4405–4423, 2020.

[30] K. Hornik, M. Stinchcombe, and H. White, "Multilayer feedforward networks are universal approximators," *Neural networks*, vol. 2, no. 5, pp. 359–366, 1989.

[31] A. Karpatne, G. Atluri, J. H. Faghmous, M. Steinbach, A. Banerjee, A. Ganguly, S. Shekhar, N. Samatova, and V. Kumar, "Theory-guided data science: A new paradigm for scientific discovery from data," *IEEE Transactions on Knowledge and Data Engineering*, vol. 29, p. 2318–2331, Oct 2017.

[32] N. Baker, F. Alexander, T. Bremer, A. Hagberg, Y. Kevrekidis, H. Najm, M. Parashar, A. Patra, J. Sethian, S. Wild, *et al.*, "Workshop report on basic research needs for scientific machine learning: Core technologies for artificial intelligence," tech. rep., USDOE Office of Science (SC), Washington, DC (United States), 2019.

[33] M. Raissi and G. E. Karniadakis, "Hidden physics models: Machine learning of nonlinear partial differential equations," *Journal of Computational Physics*, vol. 357, pp. 125–141, 2018.

[34] L. P. Swiler, M. Gulian, A. L. Frankel, C. Safta, and J. D. Jakeman, "A survey of constrained gaussian process regression: Approaches and implementation challenges," *Journal of Machine Learning for Modeling and Computing*, vol. 1, no. 2, 2020.

[35] J. Willard, X. Jia, S. Xu, M. Steinbach, and V. Kumar, "Integrating scientific knowledge with machine learning for engineering and environmental systems," 2021.

[36] C. Rackauckas, Y. Ma, J. Martensen, C. Warner, K. Zubov, R. Supekar, D. Skinner, and A. J. Ramadhan, "Universal differential equations for scientific machine learning," *CoRR*, vol. abs/2001.04385, 2020.

[37] J. S. Read, X. Jia, J. Willard, A. P. Appling, J. A. Zwart, S. K. Oliver, A. Karpatne, G. J. Hansen, P. C. Hanson, W. Watkins, *et al.*, "Process-guided deep learning predictions of lake water temperature," *Water Resources Research*, vol. 55, no. 11, pp. 9173–9190, 2019.

[38] J. Sun, Z. Niu, K. A. Innanen, J. Li, and D. O. Trad, "A theory-guided deep learning formulation of seismic waveform inversion," in *SEG Technical Program Expanded Abstracts 2019*, pp. 2343–2347, Society of Exploration Geophysicists, 2019.

[39] M. Raissi, P. Perdikaris, and G. E. Karniadakis, "Physics-informed neural networks: A deep learning framework for solving forward and inverse problems involving nonlinear partial differential equations," *Journal of Computational Physics*, vol. 378, pp. 686–707, 2019.

[40] N. Borrel-Jensen, A. P. Engsig-Karup, and C.-H. Jeong, "Physics-informed neural networks for one-dimensional sound field predictions with parameterized sources and impedance boundaries," *JASA Express Letters*, vol. 1, p. 122402, dec 2021.

[41] S. Alkhadhr, X. Liu, and M. Almekkawy, "Modeling of the forward wave propagation using physics-informed neural networks," in *2021 IEEE International Ultrasonics Symposium (IUS)*, pp. 1–4, 2021.

[42] B. Moseley, A. Markham, and T. Nissen-Meyer, "Solving the

wave equation with physics-informed deep learning," *arXiv preprint arXiv:2006.11894*, 2020.

[43] M. Rasht-Behesht, C. Huber, K. Shukla, and G. E. Karniadakis, "Physics-informed neural networks (pinns) for wave propagation and full waveform inversions," *arXiv preprint arXiv:2108.12035*, 2021.

[44] T. de Wolff, H. Carrillo, L. Martí, and N. Sanchez-Pi, "Assessing physics informed neural networks in ocean modelling and climate change applications," in *AI: Modeling Oceans and Climate Change Workshop at ICLR 2021*, 2021.

[45] T. de Wolff, H. Carrillo, L. Martí, and N. Sanchez-Pi, "Towards optimally weighted physics-informed neural networks in ocean modelling," *arXiv preprint arXiv:2106.08747*, 2021.

[46] K. Li and M. Chitre, "Ocean acoustic propagation modeling using scientific machine learning," in *OCEANS 2021: San Diego–Porto*, pp. 1–5, IEEE, 2021.

[47] R. Hecht-Nielsen, "Theory of the backpropagation neural network," in *Neural networks for perception*, pp. 65–93, Elsevier, 1992.

[48] A. G. Baydin, B. A. Pearlmutter, A. A. Radul, and J. M. Siskind, "Automatic differentiation in machine learning: a survey," *Journal of machine learning research*, vol. 18, 2018.

[49] D. P. Kingma and J. Ba, "Adam: A method for stochastic optimization," *CoRR*, vol. abs/1412.6980, 2015.

[50] M. Li, T. Zhang, Y. Chen, and A. J. Smola, "Efficient mini-batch training for stochastic optimization," in *Proceedings of the 20th ACM SIGKDD international conference on Knowledge discovery and data mining*, pp. 661–670, 2014.

[51] F. B. Jensen, W. A. Kuperman, M. B. Porter, and H. Schmidt, *Fundamentals of Ocean Acoustics*, pp. 1–64. New York, NY: Springer New York, 2011.

[52] F. Fisher and V. Simmons, "Sound absorption in sea water," *The Journal of the Acoustical Society of America*, vol. 62, no. 3, pp. 558–564, 1977.

[53] L. Brekhovskikh and Y. P. Lysanov, *Reflection of Sound from the Surface and Bottom of the Ocean: Plane Waves*, pp. 61–79. New York, NY: Springer New York, 2003.

[54] J. B. Allen and D. A. Berkley, "Image method for efficiently simulating small-room acoustics," *The Journal of the Acoustical Society of America*, vol. 65, no. 4, pp. 943–950, 1979.

[55] M. B. Porter, "The bellhop manual and user's guide: Preliminary draft," *Heat, Light, and Sound Research, Inc., La Jolla, CA, USA, Tech. Rep*, vol. 260, 2011.